ICARUS **135,** 41–63 (1998)
ARTICLE NO. IS985975

Galileo Observations of Europa's Opposition Effect

P. Helfenstein, N. Currier, B. E. Clark, J. Veverka, and M. Bell

Center for Radiophysics and Space Research, Cornell University, Ithaca, New York 14853
E-mail: helfenstein@cuspif.tn.cornell.edu

R. Sullivan, J. Klemaszewski, and R. Greeley

Department of Geology, Arizona State University, Tempe, Arizona 85287

R. T. Pappalardo and J. W. Head III

Department of Geological Sciences, Brown University, Providence, Rhode Island 02912

T. Jones and K. Klaasen

Jet Propulsion Laboratory, California Institute of Technology, 4800 Oak Grove Drive, Pasadena, California 91109

K. Magee

Sterling Software Inc., P.O. Box 70908, Pasadena, California 91117-7908

P. Geissler, R. Greenberg, A. McEwen, and C. Phillips

Lunar and Planetary Laboratory, University of Arizona, Tucson Arizona 85721

T. Colvin and M. Davies

RAND Corporation, Santa Monica, California 90406

T. Denk and G. Neukum

Deutsches Zentrum für Luft- und Raumfahrt (DLR), Institut für Planetenerkundung, 12484 Berlin, Germany

and

M. J. S. Belton

National Optical Astronomy Observatory, Tucson, Arizona 85719

Received December 3, 1997; revised April 7, 1998

During Galileo's G7 orbit, the Solid State Imaging (SSI) camera acquired pictures of the spacecraft shadow point on Europa's surface as well as a comparison set of images showing the same geographic region at phase angle $\alpha = 5°$. Coverage, obtained at three spectral bandpasses (VLT, 0.41 μm, GRN, 0.56 μm; and 1MC, 0.99 μm) at a spatial resolution of 404 m/pixel, shows a 162 × 220-km region of Europa's surface located at 30°N, 162°W. We have used these images to measure the near-opposition spectrophotometric behavior of four primary europan terrain materials: IR-bright icy material, IR-dark icy material, dark lineament material, and dark spot material. The high spatial resolution of the G7 images reveal low-albedo materials in dark spots that are among the darkest features (17% albedo at 0.56 μm and 5° phase) yet found on icy Galilean satellites. While material of comparable albedo is found on Ganymede and Callisto, low-albedo europan materials are much redder. All europan surface materials exhibit an opposition effect; however, the strength of the effect, as measured by the total increase in reflectance as phase angle decreases from $\alpha = 5°$ to $\alpha = 0°$, varies among terrains. The opposition effects of IR-bright icy and IR-dark icy materials which dominate Europa's surface are about 1.5 times larger than predicted from pre-Galileo studies. Low-albedo materials in dark spots exhibit unusually intense opposition effects (up to four times larger than bright icy europan terrains), consistent with the presence of a strong shadow-hiding opposition surge. The strengths of the opposition surges among average europan terrains system-

0019-1035/98 $25.00

atically vary with terrain albedo and can be explained in terms of the simultaneous contributions of shadow-hiding and coherent-backscatter to the total opposition effect. Coherent backscatter introduces a narrow angular contribution (<0.2° wide) to all europan terrains while the presence of a shadow-hiding contribution is revealed by the fact that the opposition surge is especially strong in low-albedo terrain materials. Stratigraphically young ridges with relatively high topographic relief exhibit anomalously weak opposition surges that could be caused by the presence of relatively coarse-grained regolith, highly compacted particulates, exposures of solid ice, or some combination of these. Very-high resolution images (22 m/pixel) of young-appearing ridges suggest that downslope wasting of particulate cover exposes more lithified ice along ridge crests and wall escarpments. We propose that over time, erosion of ridge topography accompanied by accumulation of detritus and mantling by regolith cover results in more mature ridge surfaces of increasingly lower (mature) porosity. We interpret the dark, reddish color of dark ridges and lineaments as a particulate coating of low-albedo materials vented from (or collected adjacent to) reactivated ridge-margins and within lenticulae.

Key Words: **Europa; photometry; regolith; spectrophotometry; ices; albedo; spectra; geological processes; Galileo; Voyager.**

1. INTRODUCTION

Regolith-covered planetary bodies exhibit a surge in surface reflectance as the solar phase angle (α) approaches zero–a phenomenon called the opposition effect. The angular widths and amplitudes of opposition surges are known to vary among planetary objects (cf. Hapke 1993, Verbiscer and Helfenstein 1998, Helfenstein *et al.* 1997a). Pre-Galileo telescopic observations of Europa (Domingue *et al.* 1991, Thompson and Lockwood 1992) indicated that its average global opposition surge is less than 0.2° wide—among the narrowest for any observed planetary surface. To investigate whether all europan terrains exhibit such an unusually narrow opposition effect, Galileo's Solid State Imaging (SSI) camera acquired pictures of the spacecraft shadow point on Europa's surface (Figs. 1a, 1c, and 1e) and a comparison set of images (Fig. 2) showing the same region at about $\alpha = 5°$.

This report provides an analysis of these data. We begin by defining and mapping the areal distribution of four primary europan terrain units on the basis of colors and albedos in the G7 images. We examine the opposition surge behavior of each terrain unit and demonstrate that opposition surge strengths of typical europan surface materials vary systematically with albedo. These systematic variations can be explained in terms of the relative contributions of two mechanisms that operate preferentially at small phase angles; the shadow-hiding opposition effect (SHOE), in which regolith grains occult their own shadows (cf. Hapke 1986, 1993), and the coherent-backscatter oppo-

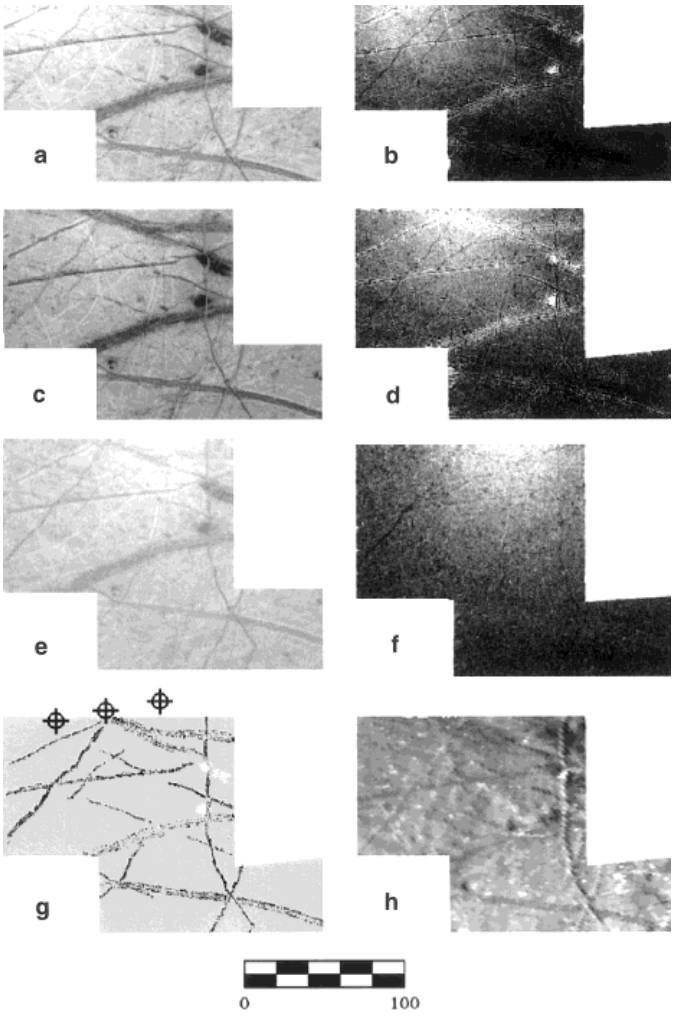

FIG. 1. (a, c, e) Calibrated G7 (G7ESVLOFOT) GRN, VLT, and 1MC images, respectively, obtained at opposition and shown at their properly scaled brightness and contrast levels. The local zone of brightening at the top of each frame centers on the Galileo spacecraft shadow point (see Fig. 1g). The brightness contrasts among geological features is strongest in the VLT and GRN images and is greatly reduced in the 1MC frame. (b, d, f) GRN, VLT, and 1MC phase-ratio images, respectively, constructed by coregistering and dividing the opposition images to their corresponding 5° phase reference images (G7ESLOWFOT, Fig. 2). The technique accentuates differences between opposition surge strengths among different europan terrains. Dark lineament and dark spot materials that have low albedos in the left images typically have large phase ratios (i.e., they appear as brighter objects in the phase-ratio images). The darkest features on Europa lie within two prominent lenticulae (Fig. 1g for locations) and also have the most intense opposition effects. Also visible in the phase-ratio images are narrow lineaments that have relatively weak opposition effects (even though their albedos are comparable or lower than those of their surroundings). (g) The location of lineaments with anomalously weak opposition effects are mapped as dark lines and features (dark areas within lenticulae) with the strongest surges shown in white. Crosshair mark shows the locations of the spacecraft shadow point in the three opposition images. (h) Near-terminator G1 CLR-filter image of the study region which has been digitally remapped to the viewing geometry of the G7 images. Spatial resolution is 1.6 km/pixel and north is up. The phase angle is 37° and features are viewed at high incidence angles (Sun toward left).

sition effect (CBOE), in which light scattered along opposing paths through small regolith grains constructively interferes (Kravstov and Saichev 1982, Shkuratov 1985, Van Albada 1985, Shkuratov 1988, Hapke 1990, Mishchenko 1991, 1992a, 1992b, Mishchenko and Dlugach 1992, 1993, Hapke *et al.* 1993, 1997). We find that stratigraphically young ridges on Europa have anomalously weak opposition surge behavior. Finally, we offer some preliminary interpretations of regolith physical properties that would be consistent with the observed range of europan opposition effects and consider implications for the geological emplacement and evolution of europan terrains.

2. OBSERVATIONS

To investigate Europa's opposition effect during Galileo's G7 orbit around Jupiter, coverage was obtained in three bandpasses[1] (VLT, $0.414\pm^{0.013}_{0.018}$ μm; GRN, $0.559\pm^{0.032}_{0.035}$ μm; and 1MC, $0.990\pm^{0.015}_{0.031}$ μm). The images (Table I) show a 162 × 220-km region of Europa's surface located at 30°N, 162°W (see Fig. 3) and provide the best spatial resolution (404 m/pixel) of any Galileo multispectral coverage for europan surface features yet obtained. Downlink limitations permitted only a portion of each 800 × 800-pixel frame to be transmitted back to Earth. Special efforts were made to accurately determine the camera pointing geometry and perform radiometric calibration. Details are provided in Appendix I.

For clarity, we have separated the following presentation into three discussions. We begin in Section 2.1 by defining four[2] important terrain materials (IR-bright icy material, IR-dark icy material, dark lineament material, and dark spot material) on the basis of their colors and albedos and discussing the relationship of these materials to terrains classified by other workers. In Section 2.2, we explore the average opposition surge behaviors of different europan terrain materials. Finally, in Section 2.3 we identify and analyze features (young-appearing ridges) that exhibit anomalously weak opposition effects in comparison to those of typical europan terrains.

Our primary data set consists of reflectance measurements extracted from calibrated Galileo frames listed in Table I as well as images constructed by combining individual frames as color composites (Figs. 2a and 2b) or as ratio images (Figs. 1b, 1d, and 1f). Table II and Fig. 2c identify the four terrain materials we investigate in Sections 2.1 and 2.2.

Average opposition surge behaviors of the terrains are illustrated in Fig. 4 as disk-resolved "phase curves"—plots showing the reflectance of the different terrains as functions of phase angle. We have fit smooth curves through these data[3] for the purposes of comparing terrain albedos at two specific phase angles ($\alpha = 0°$ and $\alpha = 5°$) and to compare the gross shapes of disk-resolved phase curves over this range of phase angles. Note, however, that our results and conclusions do not depend on the physical interpretation of photometric model parameters. Our conclusions rely only on the satisfactory ability of the photometric model to fit accurately the photometric data over a limited range incidence (31–35°) and emission angles (32–37°) and phase angles (0–5°).

Average spectral albedos of terrain units evaluated at 5° phase and at opposition, respectively are listed Table III. They are also plotted as a function of wavelength, separately at 5° phase (Fig. 5a) and at opposition (Fig. 5b). Figure 6 demonstrates how the opposition albedos of terrains vary systematically with their corresponding albedos measured at $\alpha = 5°$. In Fig. 7, we use model fits to compare the relative shapes of opposition effects for different terrains and show that their relative amplitudes significantly vary. This fact is confirmed by the nonuniform appearance of Figs. 1b, 1d, and 1f which show "phase-ratio" images constructed by dividing opposition frames (G7ESVLOFOT) by their 5° phase counterparts (G7ESLOWFOT). To measure relative amplitudes of opposition surges, we define the ratio of the opposition albedo to that measured at $\alpha = 5°$. Figure 8 shows how the relative amplitudes of different europan terrains vary in complicity with their corresponding 5° albedos.

Figures 1b, 1d, and 1f reveal linear features with anomalously weak opposition surges in comparison to average terrain materials. The locations of these features are mapped in Fig. 1g. Figure 1h is a G1 image obtained at high incidence angle and shows that the anomalous features correspond to prominent topographic ridges. Disk-resolved "phase curves" of the anomalous ridges are presented in Fig. 9, and spectral albedos are listed in Table IV.

[1] SSI bandpasses are given as effective wavelengths plus and minus a tolerance representing the bandwidth at half-maximum.

[2] Later (in Section 2.2) we identify two special subclasses of features that are covered, respectively, with dark lineament material and IR-dark icy material (see Fig. 2). The features are found to correspond to prominent narrow topographic ridges (Figs. 1g and 1h). Ridges that are covered with dark lineament material will be called "dark ridges," while those covered by IR-dark icy material will be called "IR-dark icy ridges." We discover that dark-ridges and IR-dark icy ridges have distinctly weaker opposition effects than other europan terrains.

[3] Smooth curves through the data are preliminary fits of the Hapke/Mishchenko photometric model described in Helfenstein *et al.* (1997a). This model was chosen because it contains a detailed description of both shadow-hiding and coherent-backscatter opposition effects, because it takes into account the angular size of the Sun, and because it has been applied successfully to analyze shadow-point observations of the lunar surface. Starting values of model parameters were obtained by adopting Hapke model parameters for Europa's leading hemisphere from Domingue *et al.* (1991). For each terrain, we then adjusted only the model parameters that describe the average particle albedo and the angular width and amplitude of the opposition effect to fit data over phase angles from 0 to 5°.

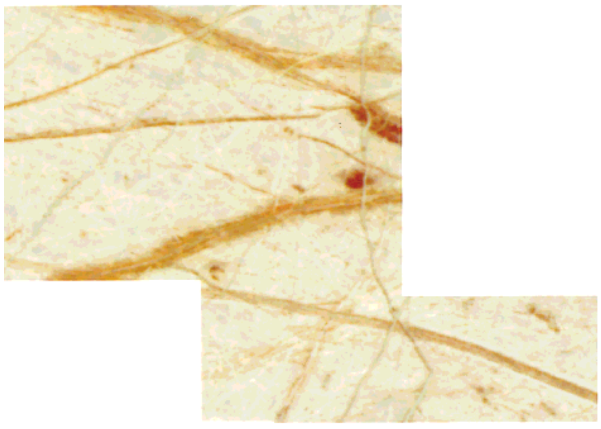

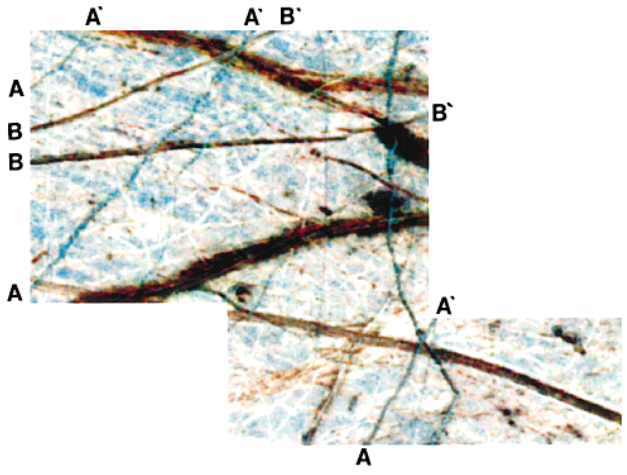

DARK SPOTS

DARK LINEAMENTS

IR–DARK ICY MATERIAL

IR–BRIGHT ICY MATERIAL

0 100

SCALE (km)

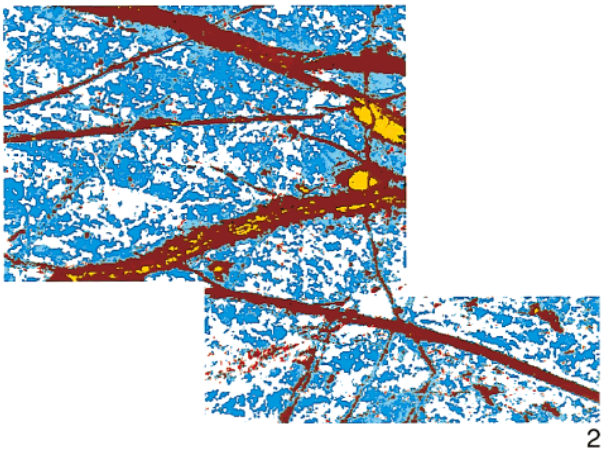

2

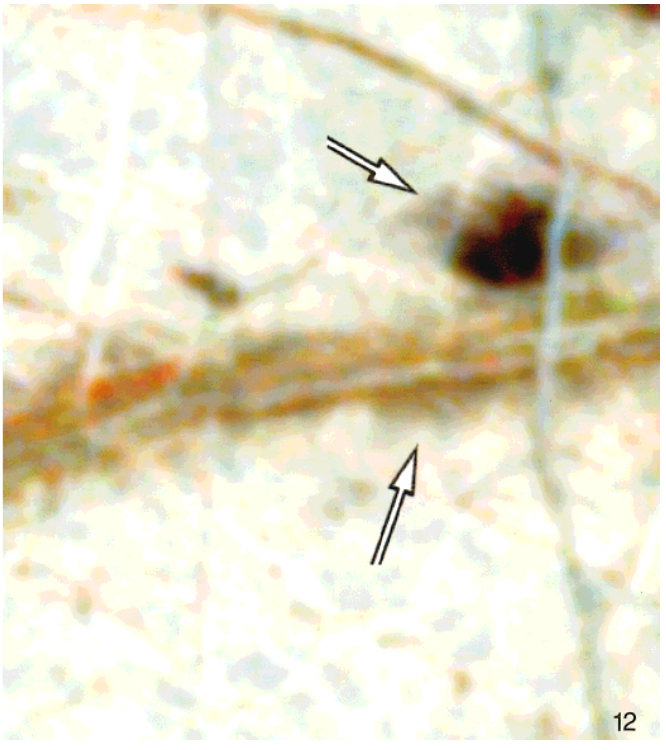

12

TABLE I
Images Used in this Study

Frame	Observation sequence	Filter	Phase	Resolution (km/pix)	Comments
S0349875113	G1ESGLOBAL	CLR (0.64 μm)	37.5°	1.585	Region near terminator shows surface topography
S0389767100	G7ESLOWFOT	GRN (0.56 μm)	4.6°	0.455	Reference GRN-filter image
S0389767113	G7ESLOWFOT	VLT (0.42 μm)	4.6°	0.455	Reference VLT-filter image
S0389767126	G7ESLOWFOT	1MC (0.99 μm)	4.5°	0.454	Reference 1MC-filter image
S0389768800	G7ESVLOFOT	GRN (0.56 μm)	0.00–0.3°	0.404	Shadow point at (line 330, sample 419)
S0389768813	G7ESVLOFOT	VLT (0.42 μm)	0.01–0.3°	0.404	Shadow point at (line 357, sample 342)
S0389768826	G7ESVLOFOT	1MC (0.99 μm)	0.03–0.3°	0.403	Shadow point at (line 400, sample 254)
VGR 2064934	1207J2-001	VIO (0.41 μm)	88.3°	1.879	Map-projected and photometrically normalized to G7 geometry for scattered light correction
VGR 2064937	1210J2-001	BLU (0.48 μm)	88.7°	1.873	Map-projected and photometrically normalized to G7 geometry for scattered light correction

2.1. Average Terrain Materials: Albedos and Colors

Color composites formed from the three G7ESLOWFOT images obtained at $\alpha = 5°$ are shown in Fig. 2. Four europan terrains can be distinguished in these images simply from their differences in color and albedo (Fig. 2, map). We adopt a classification scheme similar to that used by Belton *et al.* (1996) from their analysis of Galileo G1 color coverage. Note, however, that our classifications are not identical because (1) the G7 images fall outside the region of Europa's surface studied by Belton *et al.*, (2) the G1 images used by Belton *et al.* were obtained at a significantly higher phase angle (37°) than our G7 coverage (0–5°), and (3) the G1 color images are of four times poorer spatial resolution (1.6 km/pixel) than our G7 images (0.4 km/pixel). Also, although our choices of material unit boundaries were guided by obvious strong correlations of color and albedo with feature morphology, we have not restricted our units to be uniquely confined by specific morphological structures. Our terrain units and the ranges of 5°-phase spectral albedos that define them are listed in Table II.

Most terrains in the G7 scene are covered with bright icy materials. Figure 2 reveals two varieties, IR-bright icy material and IR-dark icy material, analogous to Belton *et al.*'s (1996) infrared-bright plains and infrared-dark plains terrains, respectively. Like Belton *et al.*'s plains units, IR-dark icy and IR-bright icy materials are distinguishable by virtue of the latter's higher albedo in the near-infrared (1 μm). However, at shorter wavelengths, Table II (see also Fig. 5) shows that they are not statistically different. (In contrast, Belton *et al.*'s infrared-dark plains are brighter in the VLT filter (0.41 μm) than their infrared-bright plains unit.) IR-bright materials are distributed as irregular patches that often define broad (up to 30 km wide) indistinct bands which are subdivided and overprinted by most other terrains. More markedly, they are also distributed in a complicated network of bright lineaments a few kilometers in width, analogous to IR-dark materials being dis-

FIG. 2. (top left) Color composite image derived by representing SSI VLT, GRN, and 1MC frames as shades of blue, green, and red, respectively. The image crudely portrays Europa's natural appearance at 5° phase. At top, right, the colors have been greatly exaggerated to accentuate subtle spectral differences between terrains. Lineaments labeled A-A′ and B-B′ are IR-dark icy ridges and dark ridges, respectively (see Section 2.2). (bottom) Map showing the areal distribution of three major europan terrain types in the scene. Table I lists the ranges of spectral reflectances that were used in the unit definitions. North is up and the smaller of the two major dark spots is Davies *et al.*'s (1998) Europa control point number 31 and is located at 29.7°N, 161.7°W.

FIG. 12. Enlargements of specific features in Fig. 2 (each frame is 50 × 50 km and north is up). (left) Brownish lenticulae (arrow) flanking young IR-dark icy ridges. (right) Diffuse, feathery appearing boundary (top arrow) of along the edge of a dark lineament. A similar diffuse deposit (bottom arrow) surrounds a prominent lenticula (e.g. Davies *et al.*'s 1998 control point 31). A subtle NE–SW trending albedo banding suggests that dark materials have preferentially collected in the troughs of subtle, small-scale surface undulations.

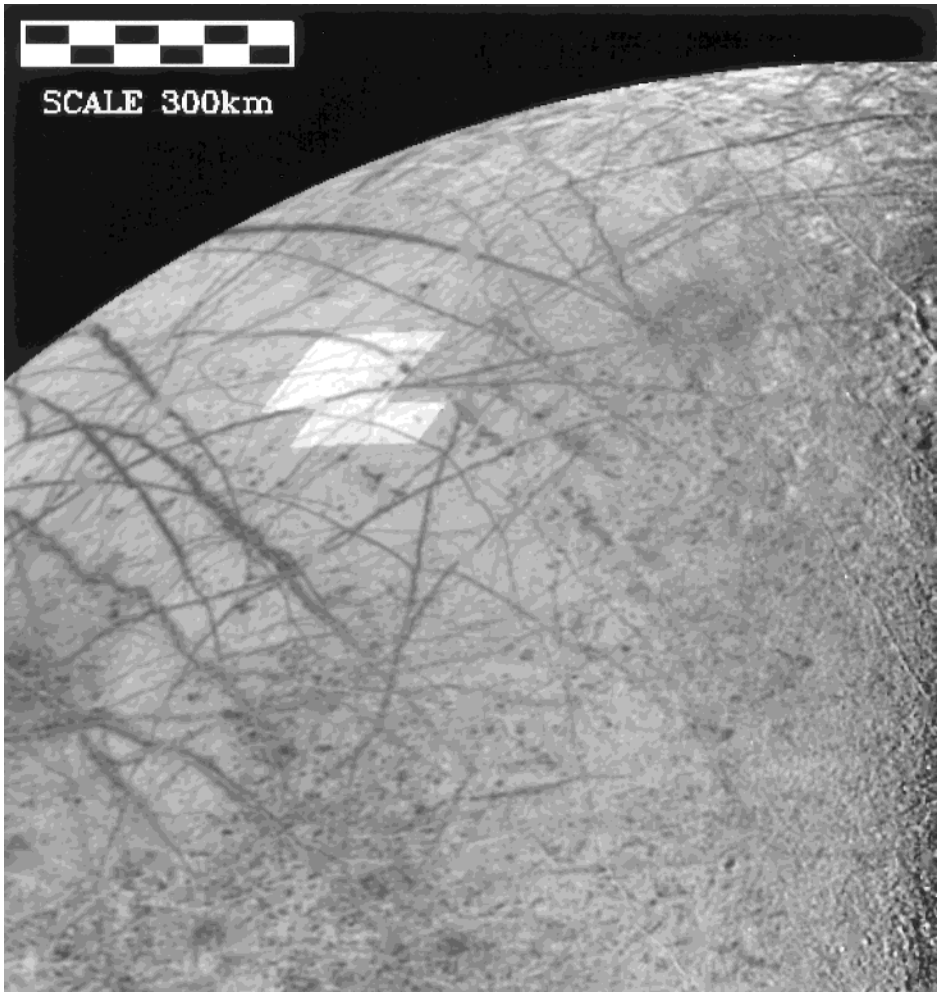

FIG. 3. Voyager violet image (20649.34, see Table I) showing the geographic placement of the G7 study region (highlighted). North is up, the spatial resolution is 1.9 km/pixel, and the center of Europa's disk is at 19.7°S, 132.6°W.

tributed similarly both as smooth plains and in narrow lineaments.

Europa's surface is transected by a variety of curvilinear albedo features, usually less than 10 km wide with albedos typically quoted as 15% darker (Luchitta *et al.* 1981) than the plains on which they are emplaced. Among morphologic variants of these features classified by earlier workers (Belton *et al.* 1997, Geissler *et al.* 1998, Clark *et al.* 1998, Luchitta *et al.* 1981, Luchitta and Soderblom 1982, Buratti and Golombek 1987) are dark bands and triple bands. We have defined our dark lineament units so that they generally correspond to dark bands and the dark portions of triple bands that appear in the G7 images. As Table II shows, the GRN-filter albedos of dark lineament materials vary significantly (by over 120%) and are intermediate in albedo and color between IR-bright icy material and dark spot material (see below).

TABLE II
Ranges of 5°-Phase Spectral Albedos Used in the Sampling of Europan Material Units[a]

Terrain material	VLT (0.42 μm)	GRN (0.56 μm)	1MC (0.98 μm)
Dark spots	0.07–0.25	0.15–0.45	0.46–0.65
Dark lineaments	0.11–0.63	0.35–0.78	0.57–0.87
IR-Dark icy material	0.50–0.80	0.71–1.00	0.68–0.80
IR-Bright icy material	0.49–0.80	0.71–1.00	0.80–0.90

[a] A small amount of overlap among the albedo ranges was allowed to account for borderline examples, usually occurring at the margins of geological features, that could equally well be assigned to either of two classes.

Dark spots are deposits of unusually low-albedo material in comparison to other materials on Europa's surface. As defined in Fig. 2, they are most widely distributed as the darkest portions of isolated lenticulae (low-albedo spots or ''freckles'' in Belton *et al.* 1996)—features which are ovate to irregular in planform and usually less than 20 km across. They also occur as very dark deposits within dark and triple bands. The spatial resolutions of previous Gali-

TABLE III
Average Albedos and Colors of Terrain Materials

	VLT		GRN		1MC		VLT/GRN			1MC/GRN		
TERRAIN	5°	0°	5°	0°	5°	0°	5°	0°	37°	5°	0°	37°
Dark spots	0.18 ± 0.07	0.48 ± 0.17	0.38 ± 0.06	0.77 ± 0.13	0.60 ± 0.02	1.09 ± 0.06	0.47 ± 0.20	0.62 ± 0.24	0.80	1.6 ± 0.3	1.4 ± 0.2	1.2
Darkest spot	0.057 ± 0.002	0.46 ± 0.01	0.17 ± 0.01	0.60 ± 0.01	0.50 ± 0.02	0.94 ± 0.04	0.34 ± 0.02	0.77 ± 0.04	± 0.12	2.9 ± 0.2	1.6 ± 0.1	± 0.1
Dark lineaments	0.59 ± 0.02	1.06 ± 0.04	0.67 ± 0.03	1.30 ± 0.06	0.73 ± 0.02	1.38 ± 0.03	0.88 ± 0.07	0.82 ± 0.07	0.76 ± 0.08	1.09 ± 0.07	1.06 ± 0.07	1.11 ± 0.10
IR-Dark icy material	0.65 ± 0.01	1.10 ± 0.02	0.80 ± 0.01	1.41 ± 0.02	0.77 ± 0.01	1.46 ± 0.02	0.81 ± 0.03	0.78 ± 0.03	0.86 ± 0.03	0.96 ± 0.03	1.04 ± 0.03	0.83 ± 0.02
IR-Bright icy material	0.64 ± 0.01	1.11 ± 0.02	0.82 ± 0.01	1.45 ± 0.02	0.81 ± 0.01	1.48 ± 0.02	0.78 ± 0.03	0.76 ± 0.03	0.81 ± 0.04	0.99 ± 0.03	1.02 ± 0.03	0.92 ± 0.05

leo and Voyager images were inadequate to resolve the lowest albedo exposures of dark spot materials. For example, the darkest examples in G1 images seen at 1.6 km/pixel resolution (Clark *et al.* 1998) have GRN-filter normal albedos of 0.77, which, for comparison with Table I data, corresponds to a 5°-phase albedo of 0.56. In G7 images, the darkest examples have significantly lower GRN-filter albedos of about 15%. Dark-materials on Callisto's surface and dark crater floor deposits on Ganymede have comparable GRN-filter albedos, however, europan dark materials are significantly redder (see Fig. 5c). We will discuss the geological significance of dark spot and dark lineament materials in detail in Section 3.3.

Tables II and III and Fig. 1 (see also Fig. 5) confirm results of other workers (cf. Clark *et al.* 1998, McEwen 1986, Buratti and Golombek 1987) who showed that albedo contrasts between most europan terrains decrease with increasing wavelength. The maximum contrast between the brightest IR-bright icy terrains and the lowest-albedo dark spot material decreases from 84% in the VLT, to 74% at GRN, to 32% at 1MC. It is important to recognize that our ability to compare colors and albedos of terrains on different parts of Europa can be influenced by the fact that terrain colors may change with phase angle. That such phase-angle dependent changes in color occur is demonstrated in Table III, where we have evaluated relative colors of terrains both at 5° phase and at opposition. Relative colors of terrains are represented in Table III by their average VLT/GRN and 1MC/GRN brightness ratios. Deviations of these ratios from unity measure how strongly colored they are. Dark spots show the greatest color change: the lowest albedo examples have VLT/GRN ratios that are 65% closer to unity at opposition than at 5° and 1MC/GRN ratios are 71% closer (i.e., they effectively become grayer at opposition). Color changes in IR-bright icy and IR-dark icy materials are more modest; however, Table III implies that at opposition, IR-bright and IR-dark terrains become statistically indistinguishable from one another.

Phase-angle dependent changes in terrain color likely extend to phase angles larger than $\alpha = 5°$. Colors and albedos of europan terrains analogous to our units measured at $\alpha = 37°$ from earlier G1 Europa images (Clark *et al.* 1998) are also given in Table III. It is important to remember, however, that G1 data were obtained at four times poorer spatial resolution (1.6 km/pixel) and over a broader region and range of terrain variants than in the relatively small G7 region. It is thus difficult to determine if any gross contrasts in color and albedo between G1 and G7 examples are due to real variations of photometric behavior of terrains with phase angle, regional heterogeneity of terrains, or the fact that small features like narrow lineaments and dark spots are more poorly resolved in G1 images than in G7. Within the statistical uncertainties reported in Table III, terrain colors observed in G1 and G7 images are generally similar and few uniform changes with phase angle are seen among them. Dark lineaments are more strongly colored at 37° phase than at 5°. The spectral distinguishability of IR-dark icy and IR-bright icy materials is also greater at 37° phase. Large uncertainties in the color ratio values for average dark spots is mostly due to the variability in albedos of different examples. The G7 dark spots at 5° phase are more strongly colored than the G1 examples at 37°, however, the difference may simply be an apparent effect of our better spatial resolution.

2.2. Opposition Behaviors of Europan Terrain Materials

In this section we measure the average shapes and relative strengths of opposition surges for each of the four terrain materials identified in Fig. 2. We examine similarities and search for differences among the opposition surges among terrains and for each terrain at different wavelengths. We are especially interested in identifying differences which show a systematic dependence on wavelength and terrain albedo because such differences can help to distinguish the relative importance of two physical phenomena that contribute to opposition behavior: the

Shadow-Hiding Opposition Effect (SHOE) and the Coherent Backscatter Opposition Effect (CBOE). In SHOE, the brightness of the surface increases with decreasing phase angle as shadows cast by particles become increasingly occulted by the grains themselves (see Hapke 1986, 1993). Because multiply scattered photons in bright surfaces tend to illuminate particle shadows and reduce contrast, the strength of SHOE should decrease with increasing surface albedo. CBOE occurs because of the preferential constructive interference of light at small phase angles from multiple wavefronts that are scattered in conjugate directions by particles or surface crenulations (see Kravstov and Saichev 1982, Shkuratov 1985, 1988, Van Albada 1985, Hapke 1990, Shkuratov *et al.* 1991, Mishchenko 1991, 1992a, 1992b, Mishchenko and Dlugach 1992, 1993, Hapke *et al.* 1993, 1997). Because the efficacy of CBOE depends on multiply scattered photons, it should be present in bright surfaces even when SHOE cannot be detected.

By comparison to the lunar photometric function, where both SHOE and CBOE have been observed in lunar shadow-point observations (Buratti *et al.* 1996, Helfenstein *et al.* 1997a, see also Shkuratov *et al.* 1997) and lunar sample data (Hapke *et al.* 1998), we anticipate that CBOE may form a very narrow contribution to Europa's total opposition effect relative to that of SHOE. In the lunar case, the angular width of CBOE is about 2° compared to over 8° for SHOE.

The three radiometrically calibrated opposition G7ESVLOFOT images (VLT, GRN, 1MC) are shown in Fig. 1. During the 17-sec interval over which the G7ESVLOFOT images were acquired, the spacecraft shadow point traversed 70 km from west to east. In each frame, a localized concentric brightening reveals the location the shadow point (see also Fig. 1g) and confirms the presence of a very narrow angular component of the opposition effect. Using the terrain map of Fig. 2 as a guide, we measured the absolute disk-resolved spectral reflectances of separate terrain types as a function of photometric geometry from the G7ESLVOFOT and G7ESLOWFOT images. Of the four terrain materials (Fig. 2), IR-bright icy and IR-dark icy are the most widely distributed and consequently the most uniformly sampled with phase angle. Sampling of dark lineaments and dark spots is less continuous in phase angle and local differences in the albedos of particular examples introduce greater scatter in the phase curve data (Fig. 3).

All of the major terrain classes exhibit qualitatively similar opposition behavior (Fig. 4). In the GRN filter, the behaviors of IR-bright icy and IR-dark icy materials are nearly identical at all phase angles shown. Europan terrains typically exhibit a gradual increase in surface reflectance as phase angle decreases from 5° to about 0.3°. Then, at $0.04 \leq \alpha \leq 0.3°$, a more extreme nonlinear surge in reflectance takes place. At 0.04°, all terrains display a conspicuous flattening toward $\alpha = 0°$.

The observed flattening near 0°, common among all of our phase curves, is predicted as a consequence both of the finite angular radius of the Sun (0.05° at Europa's mean solar distance) and the contribution of coherent backscatter (Etemad *et al.* 1987) to the opposition effect. It was first seen on the Moon in Apollo 8 photographs of the command module shadow point (Pohn *et al.* 1969, Whitaker 1969), but was curiously absent in early shadow point measurements from Clementine images (Nozette *et al.* 1994). The role of the finite angular size of the Sun in controlling the phase-curve flattening near $\alpha = 0°$ was considered by Lumme and Bowell (1981). Shkuratov and Stankevich (1995) and Shkuratov *et al.* (1997) argued that the apparent absence of the solar flattening in Clementine data brought to question the analysis methods applied by Nozette *et al.* (1994). The combined effects of flattening due to the Sun's angular size and to coherent backscatter are considered in Shkuratov (1991) and Helfenstein *et al.* (1997a). Helfenstein *et al.* (1997a) obtained satisfactory fits to the opposition flattening seen in Apollo 8 shadow-point data by taking into account both coherent backscatter and the angular size of the Sun.

The mean albedos of terrains at 5° phase and corresponding extrapolated opposition albedos are given in Table III and Figs. 5 and 6. To a good approximation, the extrapolated opposition albedos increase linearly with their corresponding albedos at 5° (Fig. 6)—a result useful for estimating normal albedos of europan terrains from images obtained at phase angles that are well outside of the opposition effect.

The relative amplitudes of terrain opposition surges can be compared by normalizing all of the phase curves to unity at $\alpha = 5°$, as is done in Fig. 7. Shown for comparison is a pre-Galileo model phase curve for Europa derived from photometry of Voyager images and Earth-based telescopic observations (Domingue *et al.* 1991). Pre-Galileo telescopic whole-disk photometry of Europa extended only to $\alpha = 0.2°$—adequate to reveal the presence of an extremely narrow opposition effect but insufficient to measure accurately its total strength. As shown in Fig. 7a, the opposition effect for bright icy terrains, which dominate Europa's surface, is about 1.5 times stronger than predicted from pre-Galileo studies. Figure 7a also shows a model phase curve for average lunar regolith (Helfenstein *et al.* 1997a). The lunar curve includes the narrow contribution observed in shadow-point observations of the lunar surface (cf. Helfenstein *et al.* 1997a, Buratti *et al.* 1996) and is corrected to account for the Sun's smaller angular size at Europa's mean solar distance. Even accounting for the Sun's small angular radius at Europa (0.05° compared to 0.27° at the Earth's distance), the narrow component of the Moon's opposition effect is broader than Europa's consistent with the interpretation that lunar regolith grains

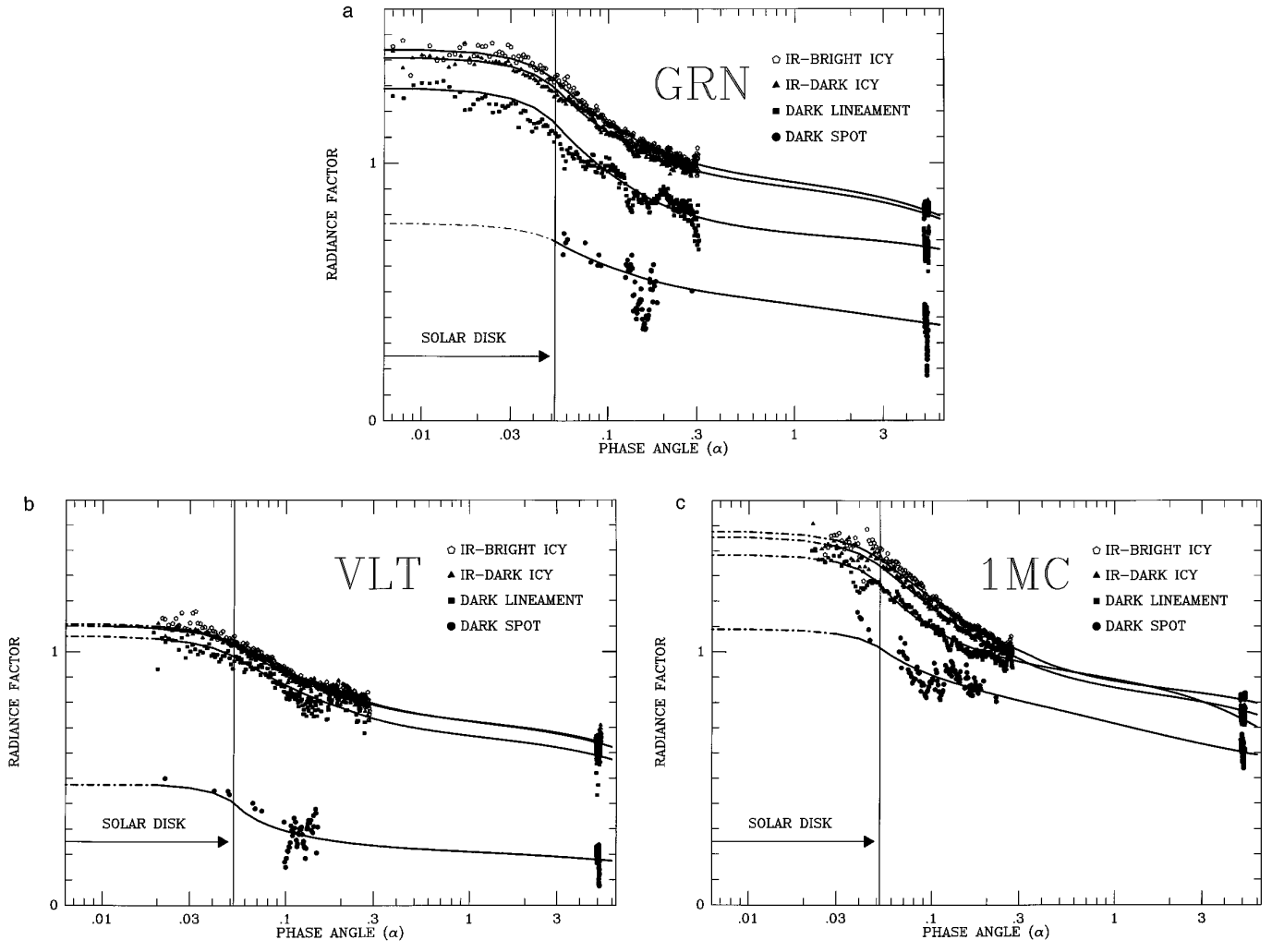

FIG. 4. (a) GRN-filter disk-resolved reflectances of four major terrains plotted as a function of phase angle. Data have been binned and averaged in 0.001° increments of phase angle. Note logarithmic scale has been used for phase angle. Curves are least-squares fits of the photometric model of Helfenstein *et al.* (1997a) to the data and accounts for the flattening of the phase curve at $\alpha = 0.05°$ caused by the finite angular radius of the Sun at Europa's orbital distance and the presence of a coherent backscatter opposition surge. Dashed line shows where the photometric model has been used to extrapolate reflectance to opposition. (b) VLT-filter disk-resolved reflectance profiles. (c) 1MC-filter disk-resolved reflectance profiles.

are more opaque than ice particles in Europa's regolith (see Section 3.1).

Figure 7 suggests a general trend; the opposition surges for relatively dark europan materials (dark lineaments and dark spots) are systematically more intense than for brighter materials (IR-bright icy and IR-dark icy materials). In Fig. 8, the relative amplitude of each opposition surge is plotted as a function of the reflectance measured at $\alpha = 5°$. The solid line is locus of relative amplitudes predicted from the linear least-squares fit from Fig. 6. The figure confirms the tendency for opposition amplitude to strengthen primarily as function of decreasing terrain albedo and reveals that shadow-hiding and coherent-backscatter both contribute to Europa's opposition surge. The presence of the shadow-hiding opposition surge is revealed by the nonlinear decrease in opposition effect strength with increasing albedo[4] (see Verbiscer and Helfenstein 1998; Fig. 4 of Helfenstein *et al.* 1997a). The presence of coherent backscatter is indicated by (1) the fact that absolute surface reflectances exceed unity at opposition but are generally less than unity at phase angles greater than 0.1° (the theoretical amplification limit from coherent backscat-

[4] For surfaces with albedos significantly larger than 20%, an additional contribution may result from the fact that the coherent-backscatter contribution should narrow with increasing particle albedo and be increasingly masked by the solar disk flattening of the phase curve (cf. Shkuratov 1988, 1991). See the discussion in Section 3.1.

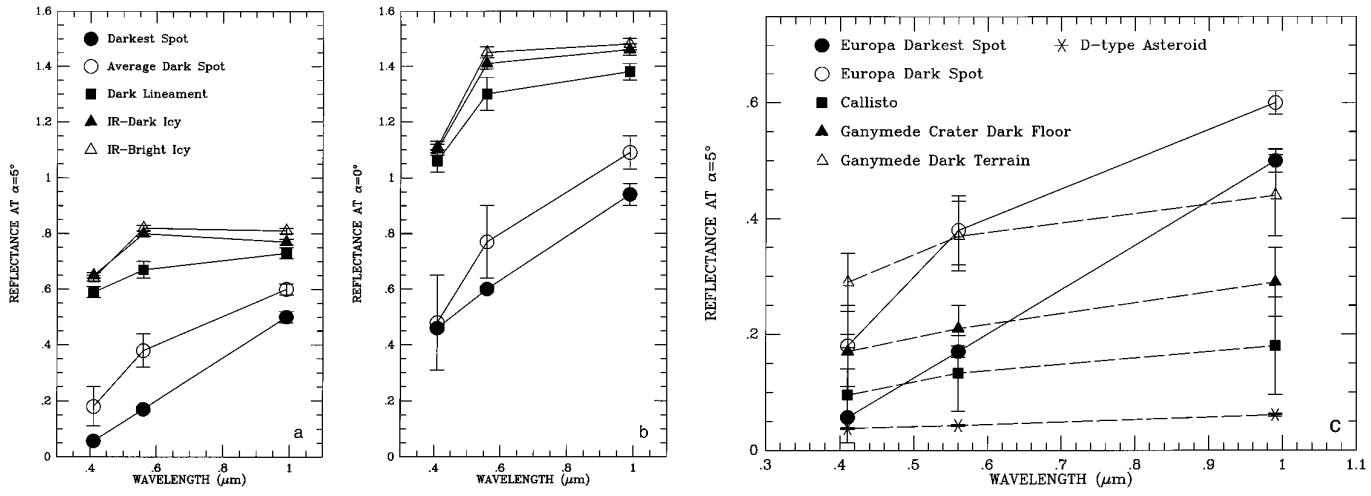

FIG. 5. (a) Absolute spectra of major terrain units at interpolated to $i = 35°$, $e = 35°$, and $\alpha = 5°$. Error bars represent the RMS error of the fit to the reflectance data. (b) Same as (a) except reflectances are extrapolated to $i = 35°$, $e = 35°$, and $\alpha = 0°$. (c) 5°-phase spectra of dark spot materials (and darkest example thereof) compared to spectra of dark materials on Ganymede and Callisto. Dark crater floor spectrum is from Helfenstein *et al.* (1997b); Callisto and Ganymede spectra are from Denk *et al.* (1997). All reflectances have been extrapolated to 5° phase ($i = e = 35°$). Ganymede spectra adopt the photometric function for Ganymede dark terrains by Helfenstein (1986). Callisto leading side photometric function of Buratti (1991) was used for extrapolating Callisto's spectrum.

ter is 2 for conservative scatterers; cf. Mishchenko and Dlugach 1992), (2) the extreme narrowness[5] (less than 0.2°) of the peaks near $\alpha = 0°$ in Figs. 3a, 3b, and 3c, and (3) the fact that the phase ratios in Fig. 8 converge to a value significantly larger than unity (1.67 ± 0.02) for the highest albedo surfaces, where shadow-hiding is most likely to be negligible (i.e., without CBOE, the phase-ratio should be closer to unity for perfect scatterers because multiply scattered light would almost completely attenuate shadows cast by particles).

[5] While coherent backscatter opposition surges can be several degrees or more in angular width (cf. Mishchenko 1992, Shkuratov *et al.* 1997, Nelson *et al.* 1998, see also Oetking 1966), in most studies where they have been identified, they are typically observed to be less than a few degrees in angular width.

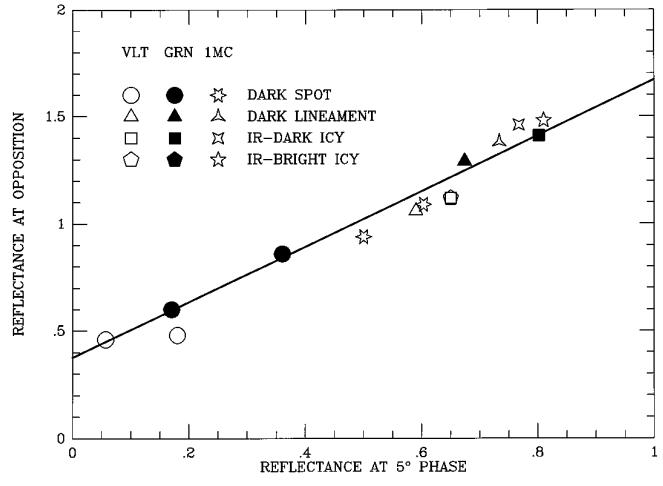

FIG. 6. Extrapolated opposition albedos of europan terrains as a function of their corresponding average brightnesses at 5° phase angle. The opposition albedos are well represented by an empirical least-squares line having a slope of 1.294 ± 0.016 and intercept 0.376 ± 0.008.

2.3. *Anomalous Opposition Surge Behavior*

In the previous section, we discovered that most europan terrains exhibit a systematic increase in opposition surge strength with decreasing terrain albedo (Fig. 8). We will consider this tendency to be representative of "normal" opposition surge behavior of europan terrains, and in what follows, we define any significant departure from this trend as "anomalous behavior." To search for anomalous opposition surge behavior among different europan terrains, we constructed "phase-ratio" images by registering the G7ESLOWFOT 5°-phase images to their opposition-phase G7ESVLOFOT counterparts and dividing the latter by the former. "Normal" opposition behavior of europan terrains is shown by the phase-ratio images in two ways. First, the narrow angular dependence of the coherent backscatter opposition effect is shown by the local surge in brightness that takes place across each image frame as the phase angle decreases from about 0.3° at the lower right edge of each frame to 0° at the shadow point. Most if not all of the terrains display similar contributions from this narrow surge in brightness; however, they are most apparent in typical IR-bright icy and IR-dark icy terrains. Second are the intense contributions from shadow-hiding opposition

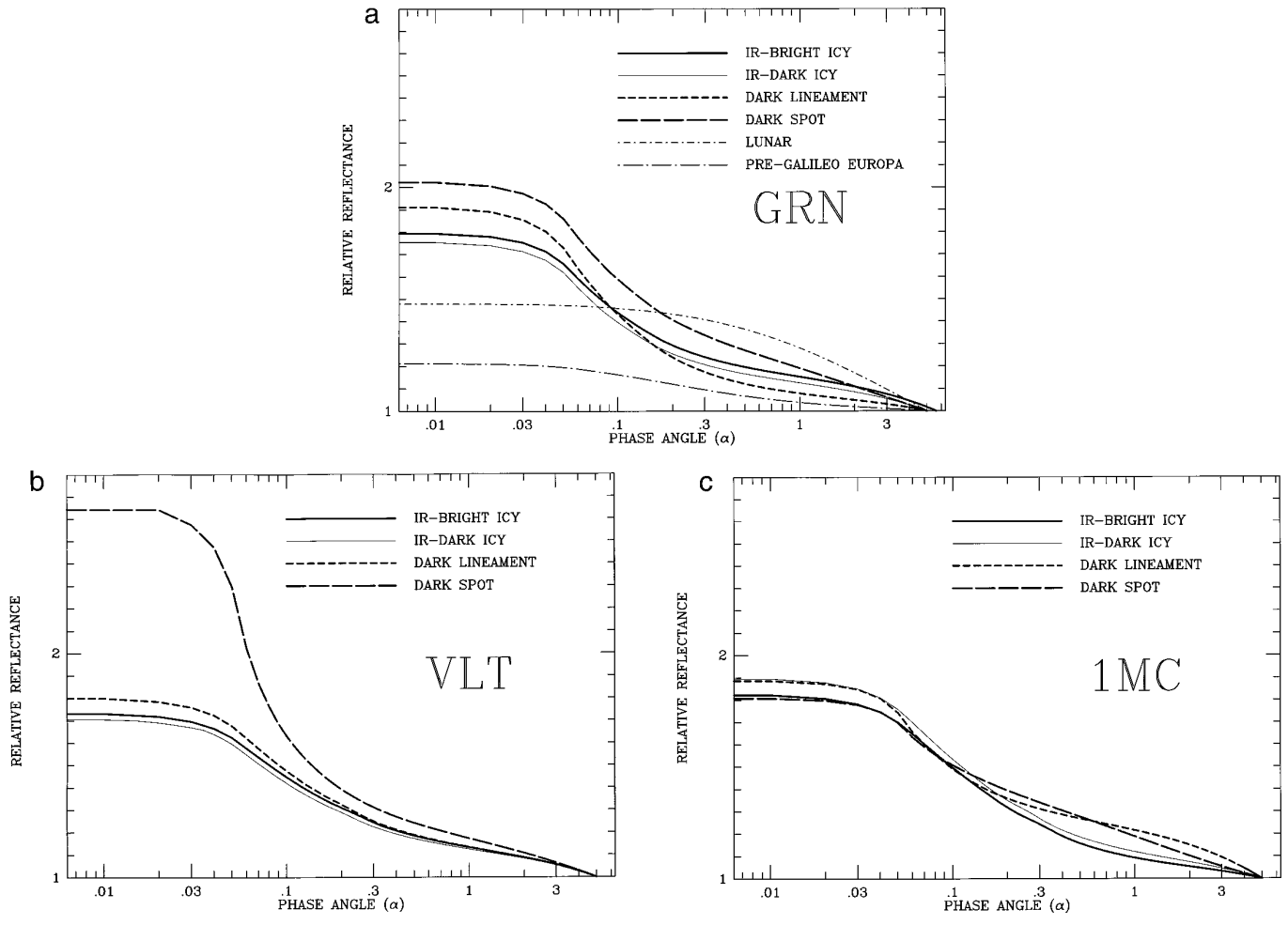

FIG. 7. Comparison of the relative amplitudes and shapes of opposition surges for different terrains at $\lambda = 0.56$ μm. The angular widths of the opposition surges for europan terrains are all broadly similar; however, the amplitudes are systematically larger for darker terrains than for brighter ones. (a) SSI GRN-filter amplitudes. The pre-Galileo Hapke model of Domingue *et al.* (1991) reasonably represents the opposition surge angular width but significantly underestimates its total strength, probably because telescopic data on which the model is based extends to phase angles no smaller than $\alpha = 0.2°$. The Moon's opposition surge (corrected for the smaller angular size of the Sun at Europa's orbital distance) is significantly broader than Europa's, consistent with the interpretation that europan regolith is more porous than the Moon's (Domingue *et al.* 1991) or, alternatively, that lunar regolith particles are more opaque than grains on Europa's surface. (b) SSI VLT-filter amplitudes, (c) SSI 1MC-filter amplitudes.

surges that occur preferentially on low-albedo terrains. This effect is most conspicuous in the GRN- and VLT-filter ratio images, where their spatial correlation to dark lineaments and dark spots is easily seen by comparison to the corresponding opposition images (Figs. 1a and 1c). Figure 1g shows the location of the most intense ratios that correspond to the darkest examples of dark spots (see Table III). In the 1MC phase-ratio images, dark lineaments and dark spots are indistinct from average surface materials. The albedo contrasts of these features with surrounding terrains are also much weaker than at other SSI wavelengths (compare Figs. 1a, 1c, and 1e).

The phase-ratio images reveal narrow lineaments that have anomalously small ratios (appear darker) than adjacent terrains even close to the shadow point. The opposition effects for these lineaments either have (1) unusually small amplitudes, (2) they are so broad that phase coverage beyond $\alpha = 5°$ is needed to fully characterize them, or (3) they are so narrow that they are masked by the solar disk flattening of the phase curve.

Comparison to Fig. 2 shows that the anomalous lineaments can be subdivided into two varieties on the basis of the materials that cover them, those composed of dark lineament material and those covered with IR-dark icy materials (see Fig. 2). To better isolate these features and map their distribution, we first removed an average bright-ice photometric function from the phase-ratio images. The main effect of this procedure was to eliminate the local

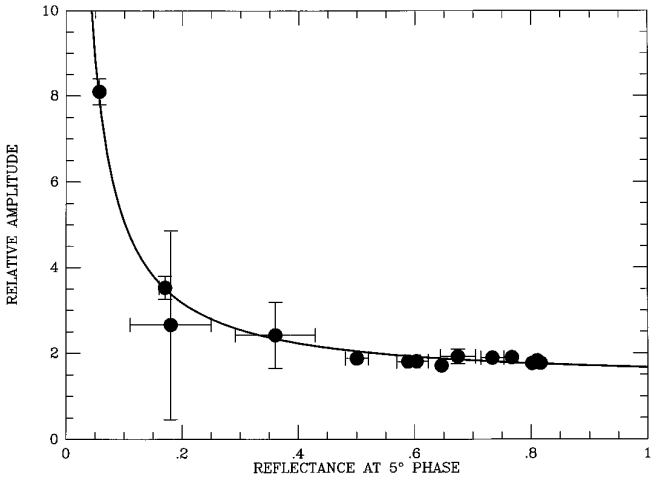

FIG. 8. Relative amplitudes of europan terrain opposition surges as a function of their average albedos at 5° phase angle. The relative amplitude is the extrapolated opposition albedo relative to the corresponding albedo of the terrain at 5° phase. The solid line is the behavior predicted from the empirical linear fit in Fig. 6. This plot indicates that both shadow-hiding (SHOE) and coherent backscatter (CBOE) opposition effects contribute to the opposition surges of europan terrains (see text for discussion). The systematic decrease on opposition surge amplitude with increasing albedo is consistent with the contribution of shadow-hiding (SHOE) to the total opposition effect. The fact that the predicted phase ratio converges to a value significantly larger than unity for the brightest surfaces is indicative of the finite contribution from coherent backscatter (CBOE).

brightening near the shadow point. We then mapped (Fig. 1g) individual examples of lineaments whose phase ratios were uniformly smaller than those for adjacent terrains. A fuller understanding of these features can be obtained from earlier Galileo coverage. The region of Europa's surface imaged in G7 was also viewed by Galileo during the G1 orbit in a single CLR-filter ($\lambda = 0.63$ μm) frame at $\alpha = 37°$ and poorer spatial resolution (1.6 km/pixel). In the overlapping G1 coverage, mapped to the G7 viewing geometry in Fig. 1h, the features occur adjacent to the terminator. At the large incidence angles ($i \approx 90°$) of G1 coverage, the surface topography of features is highlighted. Comparison of Figs. 1g and 1h shows that the anomalous lineaments correspond to small ridges, which crosscut most other features and are presumably younger in age. Hereafter, we refer to ridges that are covered with dark lineament material as ''dark ridges'' and ridges covered with IR-dark icy material as ''IR-dark icy ridges''.

Reliable phase curve data for dark ridges and IR-dark icy ridges is challenging to obtain because the ridges vary in albedo from example to example, because they are heterogeneous along strike and because of their extreme narrowness even at 404 m/pixel spatial resolution. We individually sampled brightnesses and corresponding photometric angles for each of the ridges identified in Fig. 1g. Because the albedos of ridges vary from example to example, we corrected for average ridge-to-ridge albedo differences following the method Helfenstein and Veverka[6] (1987) and combined them to obtain composite photometric data sets for dark ridges and IR-dark icy ridges, respectively. These data and corresponding smooth curve fits are shown in Fig. 9. The average albedos and colors of ridges obtained with the fits are given in Table IV.

Figure 9 shows that the narrow coherent backscatter effect is present in dark ridges and IR-dark icy ridges at phase angles less than 0.3°. The opposition effects of dark ridges and IR-dark icy ridges display the greatest differences at VLT filter wavelengths for which their albedos are also most different (41 and 54% at $\alpha = 5°$, respectively). Figure 9b shows that at $\lambda = 0.41$ μm, the dark-ridge opposition surge is significantly more peaked at $\alpha < 0.3°$ than that for the IR-dark icy ridge. In contrast, Fig. 9a shows that the opposition surges for dark ridges and IR-dark icy ridges are most similar at $\lambda = 0.99$ μm (1MC filter), where their albedos differ least (71 and 72% $\alpha = 5°$, respectively).

Tables III and IV can be used to quantitatively estimate how strongly the opposition surge amplitudes of ridges differ from other spectrally similar europan materials. We first computed the opposition amplitude (i.e., the phase ratio) for each terrain and then ratioed the opposition amplitude for the ridges relative to those of more typical europan materials. Comparing IR-dark icy ridges to average IR-dark icy material, the ratio of opposition amplitudes for VLT, GRN, and 1MC filters are, respectively, 0.96 ± 0.05, 0.91 ± 0.04, and 0.91 ± 0.05. The opposition surge amplitudes of IR-dark icy ridges are thus smaller than for typical IR-dark icy materials by less than 10%. Comparison of IR-dark ridges to spectrally similar dark lineament materials is more difficult because of the relatively large statistical uncertainties in the albedo estimates for these features. For the VLT, GRN, and 1MC filters, we obtain opposition amplitude ratios of 1.12 ± 0.15, 0.92 ± 07, and 0.99 ± 0.05. Within the estimated errors, only the GRN-filter ratio is statistically distinguishable from unity but suggests that the opposition amplitudes of dark ridges generally differ from those of spectrally similar dark lineament material by less than about 10%.

In addition to having more subdued opposition effects, ridges also have albedos lower than average europan materials of similar composition, suggesting that ridges are covered with particles of larger grain size (Belton *et al.* 1996, Geissler *et al.* 1998). A comparison of the albedos of IR-dark icy ridges from Table IV to those of IR-dark icy material in Table III shows that these ridges are signifi-

[6] This method uses a multiplicative normalization factor that adjusts the separate phase curves to have the same mean values in overlapping phase angle ranges.

TABLE IV
Average Albedos and Colors of Ridges

	VLT		GRN		1MC		VLT/GRN		1MC/GRN	
Ridge type	5°	0°	5°	0°	5°	0°	5°	0°	5°	0°
Dark ridges	0.41± 0.03	0.83 ± 0.03	0.58 ± 0.01	1.03 ± 0.01	0.71 ± 0.01	1.33 ± 0.01	0.71 ± 0.06	0.80 ± 0.03	1.23 ± 0.02	1.31 ± 0.02
IR-Dark icy ridges	0.54 ± 0.01	0.88 ± 0.01	0.70 ± 0.01	1.13 ± 0.01	0.72 ± 0.01	1.24 ± 0.05	0.77 ± 0.02	0.78 ± 0.02	1.03 ± 0.02	1.09 ± 0.05

cantly lower in albedo than spectrally similar nonridge material. A similar comparison between dark ridge albedos (Table IV) and dark lineament albedos (Table III) show that dark ridges are generally covered with relatively low-albedo examples of dark-lineament material.

3. DISCUSSION

The G7 data set have provided a variety of new discoveries whose physical and geological importance are discussed below. We first discuss the importance of the G7 observa-

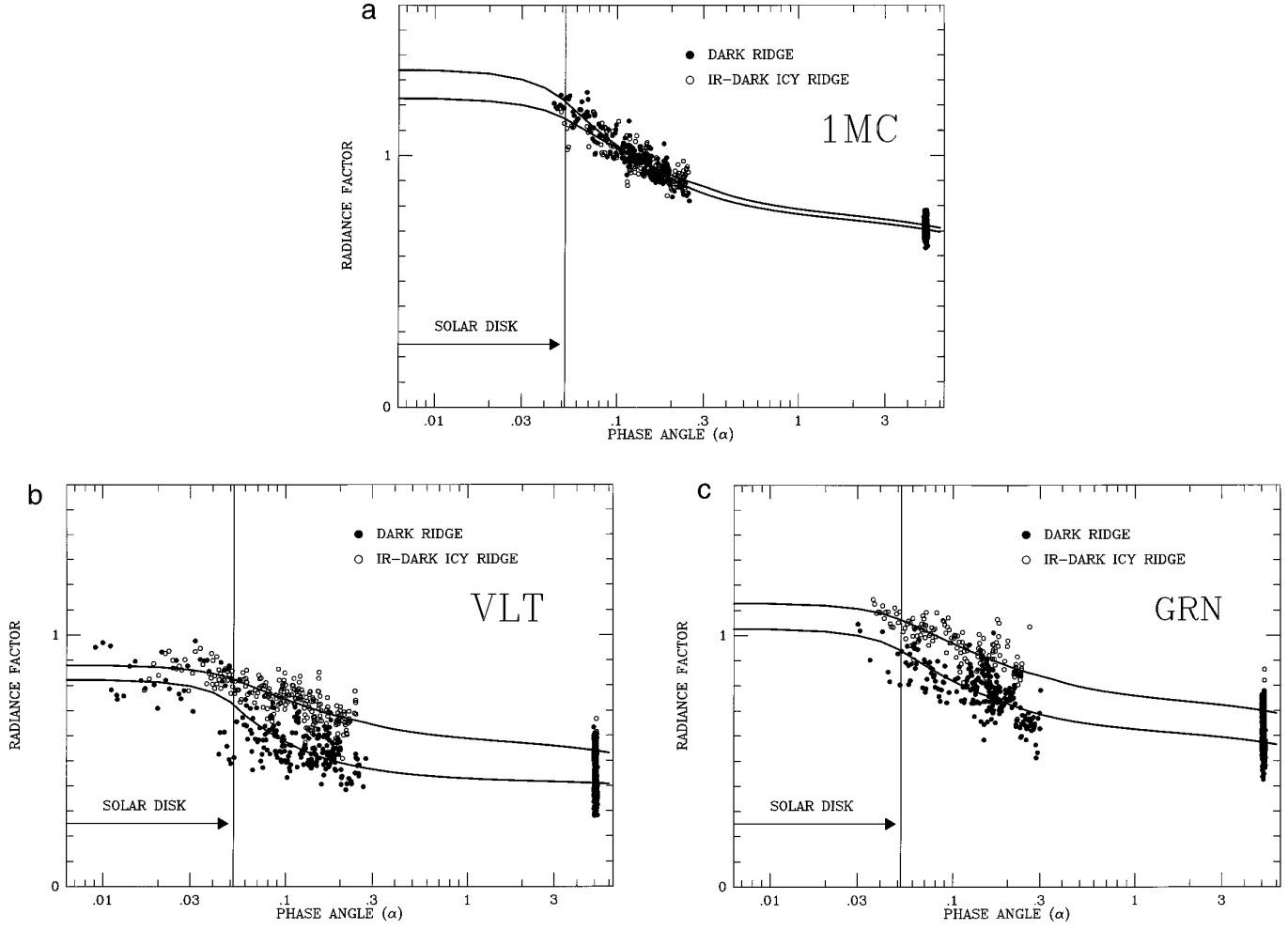

FIG. 9. Reflectances of dark ridge and IR-dark icy ridge materials as a function of phase angle. Also shown are photometric model fits (solid curves). Separate plots are given for (a) VLT-filter, (b) GRN-filter, and (c) 1MC-filter data. All ridges manifest a narrow contribution due to coherent backscatter.

tions of the opposition effect for understanding the physical properties of average europan terrain materials and those covering prominent ridges. The unusually weak opposition surges of prominent ridges is interpreted to suggest that they expose materials that are lithologically distinct from typical europan surface materials. In Section 3.2, we examine the geological setting of prominent ridges and factors that would lead to the preservation of their lithologically distinct facies. Finally, G7 images have revealed the darkest materials yet discovered on Europa's surface. In Section 3.3, we describe the geological relevance of this finding.

3.1. Regolith Properties of Average Europan Terrains and Ridges

In Section 2.2 we discovered that europan terrains exhibit both a shadow-hiding and a coherent-backscatter opposition effect. All terrains appear to exhibit a narrow ($<0.2°$ wide) coherent backscatter opposition effect whose shape is well-defined by G7ESVLOPHOT image data. The presence of the shadow-hiding contribution is revealed by the fact that low-albedo materials typically have much more intense opposition surges than high-albedo materials. The possibility that two different mechanisms (CBOE and SHOE) contribute simultaneously to Europa's opposition surge has not previously been considered. It has been shown recently that both mechanisms contribute to the Moon's opposition effect: The lunar opposition effect contains a broad ($>8°$ wide) component due to shadow-hiding and a much narrower ($<2°$ wide) contribution from coherent backscatter (Helfenstein *et al.* 1997a, Hapke *et al.* 1998, see also Shkuratov *et al.* 1996).

Until very recently, it was widely held that the occurrence of the coherent backscatter opposition effect requires the attendant presence of particles with sizes comparable to a wavelength of light (cf. Hapke 1990, Mishchenko 1992a, Hapke *et al.* 1993, Helfenstein *et al.* 1997a). However, new laboratory goniophotometry data (Shkuratov *et al.* 1997, Nelson *et al.* 1998) show that coherent backscatter can also occur in surfaces composed of very transparent particles (plausible analogs for icy particles on Europa's surface) that are much larger than a wavelength of light as well as particles that are much smaller than the wavelength of light. Additional phase coverage of our G7 study region, well outside of the opposition effect (planned for Galileo's E15-orbit), along with continued refinement of photometric theory will be required in order to draw reliable inferences about grain sizes from the coherent backscatter opposition effect. However, current theory and laboratory investigations provide a sufficient basis for proposing some possible interpretations of our results and suggest ways that they can be tested.

Current theory still supports the assertion that coherent backscatter is an interference phenomenon that requires relatively long optical pathlengths in the scattering medium and that the angular width of the coherent backscatter opposition affect should decrease in inverse proportion to the mean-free pathlength of a photon in the scattering medium (Shkuratov 1988, Akkermans *et al.* 1988, van Albada *et al.* 1990, Shkuratov *et al.* 1991). Our observations show that, at comparable spectral wavelengths, the presumed coherent backscatter component of Europa's opposition effect is significantly narrower than that for lunar regolith (Fig. 7a), even after correcting for differences in the Sun's angular diameter between the Moon and Europa. Although Domingue *et al.* (1991) have interpreted Europa's narrower opposition surge to indicate the presence of a very porous ($>90\%$) regolith, it is entirely possible that Europa's coherent backscatter opposition effect is relatively narrow (in comparison to the Moon's) because icy regolith particles are less opaque than small lunar regolith grains. Photometric constraints on the porosity of Europa's regolith require accurate estimates of the angular width of the shadow-hiding contribution. While the presence of SHOE is revealed in our G7 data, its angular width for any terrain cannot be measured without additional phase coverage that may be provided in the Galileo Europa Mission (GEM). A plausible estimate[7] of 18° for the global average angular width of a broad Europan SHOE was reported by Buratti (1985) prior to the discovery of the narrow contribution (which we attribute to coherent backscatter). Buratti (1985) interpreted this angular width to imply a surface porosity of 65%.

The opposition surges of prominent, young-appearing ridges are unusual for their relative weakness in comparison to those of more typical europan terrains. As stated earlier, this observation implies at least one of the following possibilities: The opposition effects for ridges either have (1) unusually small amplitudes, (2) they are so broad that phase coverage beyond $\alpha = 5°$ is needed to fully characterize them, or (3) they are so narrow that they are masked by the solar disk flattening of the phase curve. Additional phase coverage beyond $\alpha = 5°$ will be needed before we can uniquely determine which of these possibilities are correct. The present data set is adequate, however, to present useful limits on the range of geological conditions that might lead to the observed anomalous opposition behavior of ridges. In particular, whatever physical mechanism is invoked to account for the anomalously weak opposition effect of ridges must also account for the fact that ridges are slightly lower in albedo at all SSI wavelengths than

[7] Estimate based on the Hapke (1981, 1984) model in which the angular width, $\Delta\alpha = 2h = 0.75 \ln(P)\ Y(n(r))$, where h is the Hapke model opposition angular width parameter, P is porosity, and $Y(r)$ is a function that depends on the particle size distribution, $n(r)$. In Buratti (1985), $Y(n(r)) = 1$ is assumed.

spectrally similar europan materials that have more pronounced opposition effects.

Possibility (3), that the opposition surges of ridges are so narrow that they are masked by the solar disk flattening, is a particular case of possibility (1) and deserves special consideration. Current theoretical models of coherent backscatter (see Kravstov and Saichev 1982, Shkuratov 1985, 1988, Van Albada 1985, Hapke 1990, Shkuratov *et al.* 1991, Mishchenko 1991, 1992a, 1992b, Mishchenko and Dlugach 1992, 1993, Hapke *et al.* 1993, 1997) predict that the angular width of the coherent backscatter opposition surge should increase with decreasing particle albedo (see Section 3.1). The effect has been demonstrated in laboratory investigations, especially by Shkuratov (1988) and Shkuratov *et al.* (1991) who considered the role of the finite angular size of the light source on masking very narrow opposition effects. In the context of our Europa observations, the laboratory data of Shkuratov *et al.* (1991) suggest that coherent backscatter opposition effects of ridges could be narrow enough to be masked by solar disk flattening if the ridges are covered with particles that are significantly coarser (and hence slightly lower in albedo) than average europan surface materials. We have already found that the albedos of IR-dark icy ridges and dark ridges are indeed slightly lower in albedo than spectrally similar average IR-dark icy materials and dark lineament materials, respectively. In addition, the possibility that ridges are covered with relatively coarse-grained ice has already been proposed by Geissler *et al.* (1998) from comparison of SSI reflectance spectra of ridges to laboratory spectrophotometry of water frosts.

Possibility (2), that the opposition surge of ridges are significantly broader than 5°, would be expected of the shadow-hiding opposition effect if ridges are segregated into outcrops of solid and particulate ices, respectively, at scales too small to be spatially resolved in G7 images (i.e., at scales less than 404 m), or if particulate materials covering ridges are more compacted (less porous) than on other europan terrains (Hapke 1984, 1993). Coherent backscatter opposition effects broader than a few degrees have also been observed in laboratory experiments (cf. Shkuratov *et al.* 1997, Nelson *et al.* 1998); however, the full range of particle characteristics that lead to this result has yet to be explored.

A definitive test of the three possible explanations for anomalous opposition effects of ridges may become available during Galileo's E15 orbit of Europa, where the G7 site will be visible at a phase angle of 64° and a spatial resolution of about 200 m/pixel.

3.2. Ridges: Implications for Their Emplacement and Geological Evolution

Regardless of whether ridge opposition surges are anomalously weak due to the presence of solid ice, compacted particle grains, coarsely sorted grains, or some other property, there clearly exists some geological agent that exposes ridge material which is lithologically different than materials that cover most other europan terrains. In order for the ridge surfaces to remain lithologically distinct, they must be exposed at a rate which is faster than the rate of accumulation of a thin regolith layer that would otherwise mask them.

A useful context for relating the anomalous ridge materials to the geological environment that exposes them is provided by a very-high resolution (22 m/pixel) image returned during orbit E6 (Fig. 10c). Important structural details of ridges are identified in Fig. 10c at scales that are unresolvable in our G7 frames. For comparison to Figs. 1a–1g and Fig. 2, in Fig. 10b we have also resampled a mosaic containing the Fig. 10c region at the same spatial scale (404 m/pixel) and areal size (160 × 220 km) as our G7 images. In Fig. 10a, we have resampled Fig. 10b at 1.6 km/pixel for comparison to Fig. 1h (the scale of the G1 image from which Fig. 1h was constructed). Figure 10a reveals several conspicuous ridge systems that are similar in appearance to G7 ridge systems seen at large incidence angles in Fig. 1h. These systems range from relatively narrow ridges with the highest topographic relief (~100 m, Greenberg *et al.* 1998) to broad bands of ridges with more subdued relief. A particularly conspicuous narrow NE–SW trending ridge with high relief is identified by the arrow in Fig. 10b. This ridge compares well in scale and relief to the most prominent ridge in Fig. 1h. The closeup of this area in Fig. 10c shows that, in addition to the prominent ridge, there are numerous other ridges with much more subdued relief that transect the entire area. Most of the ridges in this frame are divided by a medial trough, the largest with relatively straight inclined walls. Vertical striations along the inward-facing scarps of the largest medial trough (labeled A) have been interpreted as scars from downslope wasting of wall debris that accumulates as talus aprons (Head *et al.* 1998, Greenberg *et al.* 1998). The flanks and distal margins of relatively young-appearing ridges are also mantled by smooth screes of apparent waste material (labeled C). The upper flanks of the ridge are terraced or divided into alternating grooves and small ridges (labeled B) on a scale of hundreds of meters in width. Terraces or grooves appear to be mantled with accumulations of dark debris. The surface structure of stratigraphically older ridges (labeled D) with subdued topographic relief is more muted by an apparent mantling of thick regolith. While talus aprons are often still visible, the older ridges lack the distinct terracing seen on young examples.

Figure 10c suggests that downslope wasting of particulate material along young, relatively high-relief europan ridges (Head *et al.* 1998, Greenberg *et al.* 1998) continually exposes fresh, solid surfaces or at least compacted, coarsely grained immature regolith along ridge crests and terrace

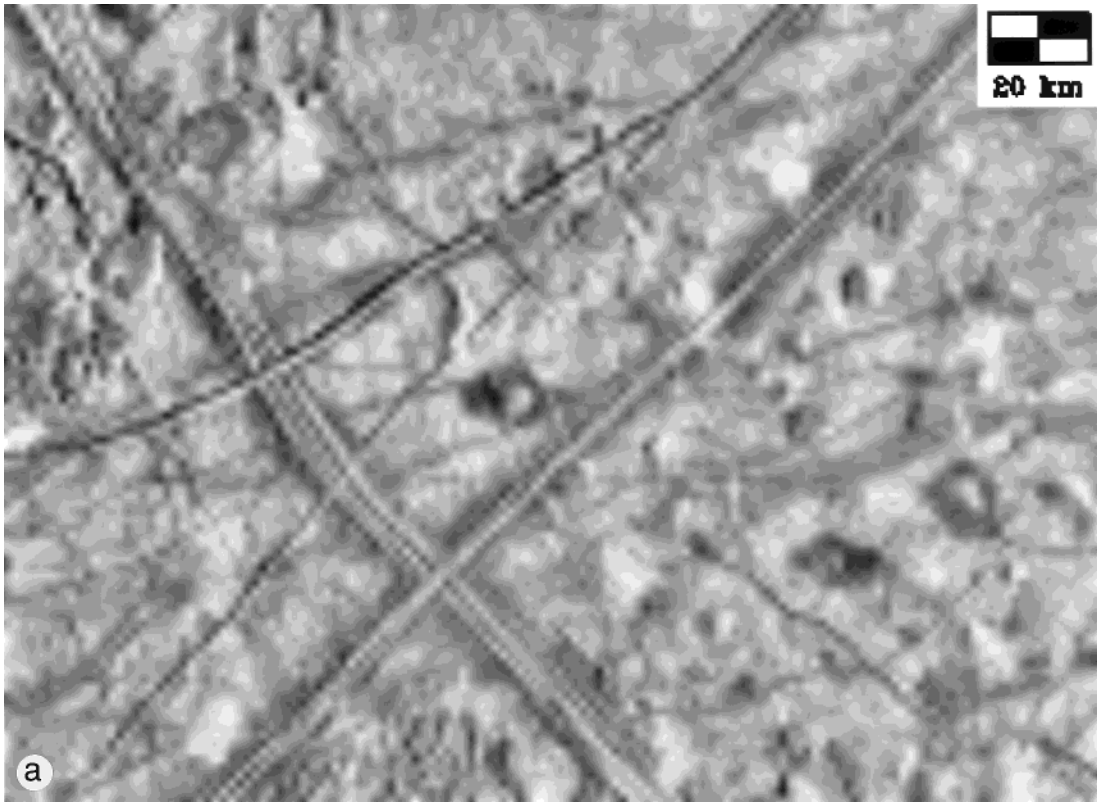

FIG. 10. (a) Mosaic of E6 images showing prominent europan ridges located near 15°N, 273°W at high incidence (78°) angle. The mosaic has been cropped to show the same amount of area (220 × 162 km^2) as the images in Fig. 1 and has been scaled to show the appearance of the ridges at the same spatial resolution (1.6 km/pixel) as Fig. 1h. North is up and illumination is from the right. (b) Same as Fig. 10a except the mosaic has been resampled to the same spatial resolution (404 m/pixel) as images in Figs. 1a–1f. Arrow shows the location of the high-resolution image in Fig. 10c. (c) High-resolution (22 m/pixel) E6 image showing detailed structure of ridges on Europa. (A) Vertical striations along walls of medial groove are interpreted as scars from mass wasting. (B) Smooth-appearing material along distal margins of ridges are detritus screes that have accumulated downslope. (C) Relatively fresh-appearing ridge exhibits terraced flanks. Smooth material appears to have deposited on horizontal terraces while terrace walls appear rough. (D) Soft, muted appearance of stratigraphically old ridges indicate that they are completely mantled by a thick regolith layer.

walls. An important demonstration that this process is detected in our phase-ratio images is seen in Fig. 11, where a prominent N–S trending ridge (see Fig. 1h) passes through very low-albedo dark spot materials in two different lenticulae. In the phase-ratio image (Fig. 11, right) the ridge is divided into three bands: two parallel bands with small phase ratios (i.e., that appear dark) separated by a medial stripe that exhibits large phase ratios (i.e., that appear bright) like dark spot material flanking the outside of the ridge. Figure 10b suggests that the medial valley of prominent ridges should easily be two or three pixels wide in Fig. 11 (about the same size as the parallel band separation in the phase-ratio image). A simple explanation for the appearance of the ridge in Fig. 11 is that particulate material has moved downslope from ridge crests, both on their outside flanks and into a medial valley that separates them. An intense shadow-hiding opposition surge is present where dark particulates have accumulated downslope but is absent where particles have wasted off of ridge crests.

Mass wasting can easily explain why young (IR-dark icy ridges) may be composed of compacted materials that are not spectrally (i.e., compositionally) distinct from adjacent IR-dark icy plains materials. In this interpretation, porous, particulate detritus derived from the mechanical disaggregation of solid outcrops simply accumulates along the ridge flanks, in between ridge terraces, and in medial valleys. However, the fact that dark-ridges are spectrally distinct from IR-dark icy ridges requires additional explanation. One obvious possibility is that IR-dark icy ridges are derived directly from icy crust material, while dark-ridges are either derived from (or covered by) dark volcanic materials extruded through (or vented from) fractures, or deposited by disintegration or thermal alteration of surface materials (Moore *et al.* 1998; Pappalardo *et al.* 1997).

Geissler *et al.* (1998) and Head *et al.* (in preparation) identified a range of morphological and spectral classes of europan ridges and lineaments and proposed that they represent different stages of a continual sequence of frac-

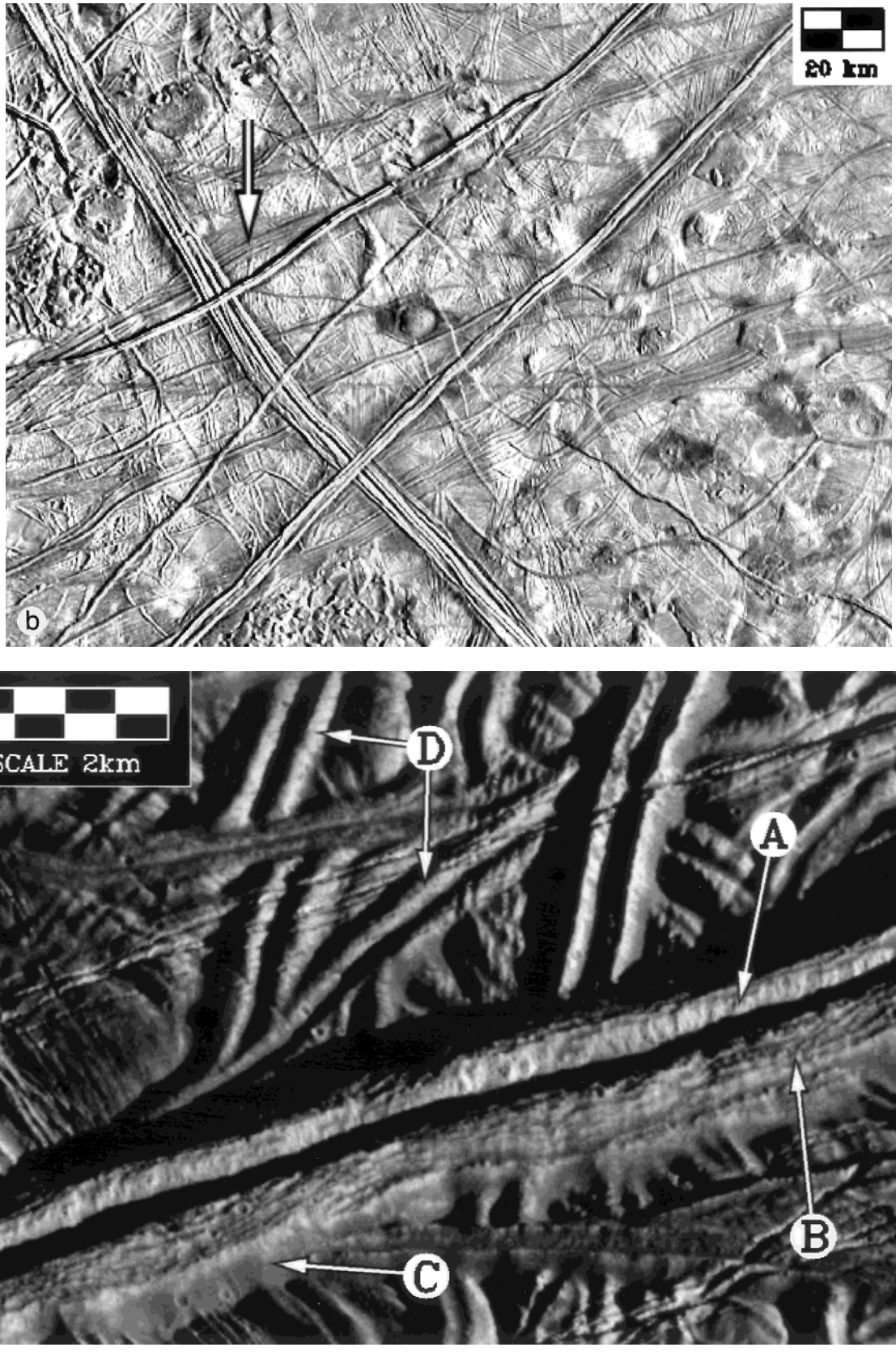

FIG. 10—*Continued*

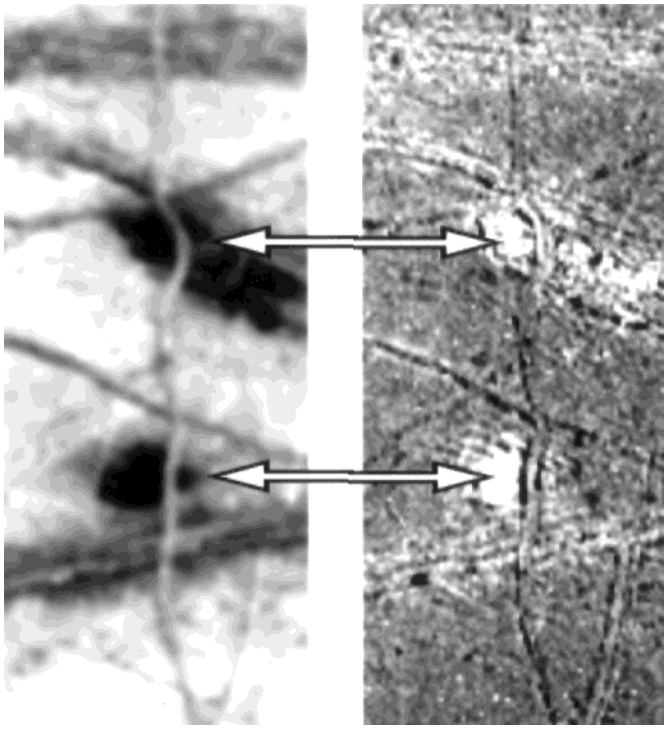

FIG. 11. Enlargements of Fig. 1c (left) and 1d (right) which show a prominent N–S trending ridge that passes through two dark lenticulae (North is up). Left side is a VLT-filter albedo image of the scene and at right is the corresponding phase-ratio image. Phase ratios are large (bright in the right image) wherever dark material with a strong shadow-hiding opposition surge is exposed (arrows). Where the prominent ridge passes through the dark spots, two parallel segments with anomalously small phase ratios (dark in the right image) are present suggesting that the dark spot material has migrated downslope and accumulated on either side of the ridge crests and in the medial valleys.

ture evolution. The fact that dark ridges are spectrally similar to adjacent dark lineament material (in the same way that IR-dark icy ridges are spectrally similar to adjacent IR-dark icy surfaces) implies that all ridges on Europa are affected by similar mechanical erosion processes and that their opposition behaviors (and regolith compaction states) evolve with time in qualitatively similar ways. Young ridges appear to express the largest topographic relief and are most likely to present clean, lithic surfaces with distinctly weak opposition effects along escarpments and ridge crests. Over time, ridge topography becomes more relaxed by virtue of erosion by mass wasting and impact abrasion, ablation, and perhaps other processes (Moore *et al.* 1998) and ridge surfaces become increasingly mantled by fluffy particulate until their opposition behavior ceases to be distinct from surrounding materials.

The geological mechanisms responsible for the emplacement of europan ridges are poorly understood and a wide variety of hypotheses have been suggested. Most (but not all) of them follow from the premise that europan ridges are topographic expressions of ice or liquid that has been extruded from or intruded into crustal fractures. Early Voyager-based models especially focused on the formation of the central stripe in triple bands. Malin (1980) noted that, in Voyager images, the central stripes of triple bands appear as ridges when viewed near the terminator. Finnerty *et al.* (1981), Ransford *et al.* (1981), and Luchitta and Soderblom (1982) suggested that central ridges in triple bands formed by intrusion of clean ice into the centers of dark, silicate dikes penetrating Europa's icy surface. Golombek and Bruckenthal (1983) proposed that the central stripes were uplifted horsts rather than icy intrusions. This hypothesis was later supported by Buratti and Golombek (1987) on the basis of the similarity in albedo of the central stripes of triple bands and bright plains materials. Cuspate ridges (Smith *et al.* 1979) were identified as relatively clean-ice relief features and postulated to be compressional features analogous to pressure ridges in terrestrial pack ice (Luchitta *et al.* 1981).

The advent of high-resolution multispectral Galileo images have rendered some of the early models unlikely. Central features in triple bands are clearly not horsts, and diffuse dark deposits along their boundaries show that they are not simply silicate intruded fractures (Ransford *et al.* 1981, Finnerty *et al.* 1981). Greeley *et al.* (1998) propose that ridges are ramparts of water ice, slush, and frost which progressively accumulate adjacent to fractures through which water, ice, and nonice contaminants erupt, driven by expanding water vapor and exsolving gasses. Head *et al.* (1998) alternatively proposed that Europa's ridges originate by intrusion of thermally induced diapiric walls that have risen along cracks. Vertical deflection and uplift of the crust flanking the cracks is proposed to occur early on and ridges subsequently grow in width as a consequence of continued intrusion from localized diapiric upwelling. Another model by Greenberg *et al.* (1998) asserts that cyclic tidal flexure of the europan crust pumps warm subsurface materials into preexisting, tidally reactivated faults. Ridge topography then arises in a manner similar to that observed in terrestrial leads, where ridges accumulate from repeated crushing of newly formed ice within fracture (lead) openings.

Our results offer new constraints on the likely modes of emplacement of ridge materials. Geissler *et al.* (1998) encountered stratigraphically young examples of europan ridges that exhibit deeper spectral absorptions in the 1-μm band than surrounding icy plains materials and conclude that they were extruded as relatively clean, coarse-grained ice particles (cf. Greenberg *et al.* 1998, Greeley *et al.* 1998). Our results are generally consistent with that interpretation. However, it is not necessary that the coarse ridge ice be freshly extruded from Europa's interior. Structural uplift of the crust adjacent to fractures, as proposed in the Head *et al.* (in preparation) model, could lead to downslope wasting of particulate cover and would expose solid ice or

a previously buried coarse, compacted particulate layer. As mentioned earlier, such a scenario accounts for the spectral similarity if IR-dark icy ridges to adjacent icy plains materials and is supported by high-resolution imaging (Fig. 10c).

Whether or not ridge formation is an ongoing geological process today is an important question for establishing the possible existence of a subsurface liquid water ocean. Our results do not provide a unique answer, but offer important clues. If ridges are emplaced as solid ice or compacted ice grains, then persistence of their anomalously weak opposition effect suggests that regolith-forming processes have been at work long enough to disrupt the exposed surface into large grains but has not progressed to the point of producing a porous, fluffy regolith like that on more mature europan terrains. Monte Carlo simulations of regolith formation on other icy Galilean satellites (Veverka *et al.* 1986) suggest that horizontal 1-mm thick porous regolith layer could easily form on time scales less than tens of thousands of years. As seen in Fig. 10, however, even on youthful examples of ridges, downslope migration of particulate material over time continually exposes fresh surfaces or immature regolith along ridge scarps and terrace walls, so a considerably longer period may be required for a uniform mantle of regolith to accumulate over all of their surfaces. The exposed compacted icy material on young IR-dark icy ridges may be older still if they represent previously buried crust that has been upwarped by diapiric upwelling (Head *et al.*, in preparation) or tectonic compression (Sullivan *et al.* 1997).

3.3. Geological Significance of Endogenic[8] *Dark Materials on Europa*

In Section 2.1 we identified exposures of dark spot material that are the lowest albedo, reddest deposits ever found on Europa's surface, and in Section 2.2 we documented their distinctly intense opposition surge behavior. Also, in Section 3.2 we noted that some explanation is needed for the emplacement of low-albedo, spectrally distinct materials on dark ridges compared to IR-dark icy ridges whose composition is similar to surrounding IR-dark icy plains. Our discovery, characterization, and interpretation of very low-albedo dark spot material is especially important because (as summarized below) dark materials appear to play a significant role in the evolution of globally distributed geological features, while their specific origin and nature has yet to be understood. Our G7 data provide the opportunity to characterize a relatively pure sample of an important europan geological material.

The composition of low-albedo material on Europa's surface remains uncertain. Fanale *et al.* (1998) report that Galileo infrared spectra of europan dark materials are dominated by hydrated minerals (clays or hydrated salts), while their redness in visible and UV spectra require an additional contaminant, such as an allotrope of sulfur. Although the darkest examples in our G7 data are comparable in albedo to dark materials on Ganymede and Callisto at $\lambda = 0.56$ μm (Fig. 5c), Europa's dark spot materials are much redder. D-type asteroid material is sometimes proposed as a possible dark contaminant in icy Galilean satellite regoliths because D-asteroids have very low albedos, because they are relatively red in color, and because they occur near the orbit Jupiter. As Fig. 5c shows, europan dark spot material is as dark as D-type asteroid material in the VLT (0.41 μm), but the spectrum of D-type asteroid material better matches those of dark materials on Ganymede and Callisto than the much redder dark spot materials on Europa.

While our designated separation between dark spot and dark lineament material was guided by the occurrence of the darkest deposits near the centers of large lenticulae, it is otherwise arbitrary and it is entirely possible that dark spot and dark lineament materials are related. Other workers (Buratti and Golombek 1988, Clark *et al.* 1998) have demonstrated that dark lineaments are well represented as mixtures of bright-icy materials (both IR-dark and IR-bright) and dark material in lenticulae analogous to our average dark spot material. This view is supported by the broad, overlapping ranges of albedos and colors that define dark lineaments and dark spots in Table II. In addition, Fig. 2c shows that small (sub-kilometer-scale) deposits indistinguishable from average dark spot materials occur in the interiors of dark lineaments, especially near medial dark ridges within them (see Fig. 1h). Similarly, materials near the margins of the two prominent lenticulae in G7 are indistinguishable in color and albedo from dark lineament materials. We conclude that dark spot material and dark lineament materials likely represent different mixes of the same compositional end-members. The darkest examples of dark-spot material (Table III) provide a better representation of the properties of a dark europan regolith compositional end-member than the examples used by other workers.

Lenticulae, dark bands, and triple bands are morphologically distinct geological features. Because they are covered by spectrally similar materials it is reasonable to suspect that dark deposits associated with them have similar origins. There are at least four current hypotheses for the

[8] McEwen (1986) isolated two distinct darkening agents on Europa's surface in Voyager multispectral maps. He modeled Europa's gradational *exogenic* leading/trailing hemispheric darkening and coloration due to implantation of dark contaminants from Jupiter's magnetosphere and subtracted it from Voyager albedo maps. The remaining dark albedo markings were interpreted to be *endogenic* because they occurred locally as dark lineaments and other features of probable tectonic and/or volcanic origin. This interpretation is supported by recent Galileo multispectral observations of Fanale *et al.* (1998). In our discussion, we focus only on the proposed *endogenic* materials.

emplacement of dark surface deposits on Europa: (1) they may represent pyroclastic fallout or flows from volcanic eruptions along fissures and isolated vents (cf. Greeley *et al.* 1998), (2) they may be lag deposits that remain after volatile ices have sublimated away over warm, near-surface thermally induced diapirs (cf. Head *et al.* in preparation), (3) they may be extrusions from diapirs that have breached the surface or extrusions of low-viscosity material resulting from partial melting of salt-rich pockets near warm diapirs (Pappalardo *et al.* 1998), (4) they may result from the disintegration (via sublimation) of mass-wasted detritus from topographically raised relief, for example, from ridge crests (cf. Moore *et al.* 1998). Whatever mechanisms operate to deposit endogenic dark materials on Europa must account for their distinct colors and albedos, their surface physical properties implied from photometry, their distribution in areal extent and thickness with respect to related geological constructs, and the way their presence affects the appearance of related geological features locally and over time.

The results from this study support the interpretation that europan dark materials represent a particulate coating on preexisting or cogenetic surfaces—an interpretation supported by recent Galileo PPR studies (Spencer *et al.* 1998) . That dark deposits are particulate in nature is indicated by the fact that dark spot and dark lineament materials exhibit detectable shadow-hiding opposition surges. Additional evidence that dark deposits are particulate is seen in Fig. 12 (right), which shows that the distal margins dark lineaments and also lenticulae often have a diffuse, wispy appearance suggesting that they gradually thin with increasing distance from the features. Near the limit of resolution in Fig. 12, the diffuse deposits exhibit a NW–SE trending banding indicating the occurrence of ridges with subdued topographic relief (like mantled ridges in Fig. 10) whose presence at this resolution and illumination geometry is detectable only by virtue of the downslope accumulation of dark particles in topographic lows.

The feathery, indistinct albedo boundaries of dark lineaments and triple bands are interpreted by Greeley *et al.* (1998) to indicate that endogenic dark material vented or erupted as a spray from fracture margins. Some of the highest resolution images of europan ridges show evidence of dark material accumulating in topographic depressions along ridge margins; however, it is unclear whether the dark material continues with depth or if it just forms a coating (like a lag deposit) on the surface of the features. Recent studies (Pappalardo and Sullivan 1996, Belton *et al.* 1996, Geissler *et al.* 1998) indicate that dark bands and the low-albedo parts of triple bands brighten with increasing stratigraphic age. Geissler *et al.* (1998) observed that the temporal optical brightening proceeds from the outer boundary of the lineaments inward, as would be expected from regolith gardening with underlying ice of a ballistically emplaced dark particulate coating that thins toward the distal lineament margins, or alternatively, by comminution of grains that are sorted to decreasing grain sizes at increasing distances from the ridge margins.

The suggestion that low-albedo deposits are derived from the disintegration of mass-wasting debris derives from very high-resolution (22 m/pixel) images of prominent ridges and associated mass wasting deposits (see Fig. 10). At the large incidence angle (78°) of the E6 coverage it is difficult to determine the full lateral extent of dark deposits around the prominent ridge in Fig. 10b; however, outward-facing detritus slopes flanking the ridge appear to be covered with or composed of dark material (Fig. 10a). In very low-resolution (6.9 km/pixel) multicolor G1 images of the area, the ridge appears as a dark lineament; however, spatial resolution needed to distinguish whether low-albedo deposits are confined to mass-wasting debris flanking the ridges awaits high-resolution multicolor coverage of the feature planned for the E12 encounter. Close examination of IR-dark icy ridges in Fig. 12 (left) shows that they are often heterogeneous along strike; near the limit of resolution, small (sub-kilometer-scale) deposits of brownish dark lineament materials intermittently dot the edges of IR-dark icy ridges, suggesting sporadic localized venting or pooling of dark materials along reactivated fracture margins rather than uniform intrusion of dark slurries into fractures, formation of a dark lag deposit from the disintegration of ridge detritus, or thermal segregation of a dark surface lag deposit by warm diapirs beneath ridges. Geissler *et al.* (1998) also noted such localized brownish deposits along the margins of Agenor linea—a conspicuously youthful candidate for possibly ongoing ridge emplacement.

4. CONCLUSIONS

G7 observations of the Galileo spacecraft shadow point on Europa's surface reveal that both shadow-hiding and coherent backscatter opposition effects contribute to the photometric behavior of materials on Europa's surface. The relative strength of each of these contributions is found to vary among terrains. All europan surface materials exhibit a narrow (less than 0.2° wide) coherent backscatter opposition surge. The coherent backscatter component of Europa's opposition surge is narrower than that for lunar regolith, even after accounting for the Sun's larger angular size at the Moon than at Europa. This difference is consistent with the fact that icy europan regolith particles are more transparent than lunar regolith grains and does not require unusually large surface porosities. A significant shadow-hiding opposition effect is also detectible by virtue of the fact that its strength in low-albedo (~6%) materials is dramatically larger than more typical high-albedo Europan terrains.

Stratigraphically young ridges with relatively pronounced topographic relief exhibit anomalously weak opposition surges in comparison to other europan terrains that have similar spectral properties. Possible explanations are that the ridges are covered by relatively coarse regolith grains, compacted particulates, exposures of solid ice, or any combination of these. If ridges are emplaced as solid ice or compacted ice grains, then persistence of their anomalously weak opposition effect suggests that regolith-forming processes have been at work long enough to disrupt the exposed surface into large grains but has not progressed to the point of producing a porous, fluffy regolith like that on more mature europan terrains. We find strong evidence, however, to show that downslope migration of particulate matter over time continually exposes fresh surfaces or immature regolith at ridge escarpments and crests.

The high spatial resolution of G7 images revealed the lowest albedo materials yet discovered on Europa's surface. These materials occur in the centers of previously identified lenticulae and have GRN-filter (0.56 μm) albedos of only 17% at $\alpha = 5°$. In the VLT filter (0.42 μm), the darkest europan materials have albedos comparable to D-type asteroid material (6% albedo at $\alpha = 5°$); however, europan dark materials are much redder than D-asteroid materials or low-albedo deposits on Ganymede and Callisto. We suggest that dark materials in lenticulae, along dark lineaments, and on dark ridges represent low-albedo particulate coating on preexisting or cogenetic terrains.

Additional photometric analysis and modeling of icy regolith evolution may help to distinguish the lithology of ridge surfaces and perhaps place absolute age constraints on ridges and ridge formation as a possibly ongoing geological process. Such analyses will benefit greatly from very high-resolution imaging to be returned during the upcoming Galileo Europa Mission (GEM).

APPENDIX I

Image Navigation and Radiometric Calibrations

A.1. Image Navigation

Especially accurate camera pointing information was needed to determine the exact location of the shadow point in each image. A pointing error of only 0.01° yields a corresponding 17-pixel error in the predicted location of the shadow point. To achieve the required camera pointing accuracy, we employed recently improved geographic control-point data for features on Europa (Davies *et al.* 1998). Our procedure was first to accurately navigate lower resolution Voyager frames (Table I, Fig. 3) that showed the areal context of the G7 images relative to surrounding features. We then identified 14 features within the G7 image that could be identified in the context frames and used as navigation tie points. Fortuitously, a prominent feature in the G7 images that we used as a tie point also corresponds to one of the standard Europa control points (see Fig. 12). From careful determination of camera-pointing geometry, we determined that the spacecraft shadow point is visible only at the margin of the GRN-filter frame and is slightly outside data margins in the subsequent VLT and 1MC images (Fig. 1g). Using Davies *et al.* (1998) control point 31 as a reference, we estimate that we have determined the location of the spacecraft shadow point to within two pixels.

A.2. Radiometric Calibration

Photometric calibration of the Galileo images was performed using standard image calibration software to convert raw image DN's into radiance factors. The JPL Multimission Image Processing System (MIPS) GALSOS program was used to implement dark current subtraction, blemish removal, and flat-field correction. Uncorrected radiation noise was removed (replaced by boxcar averages) with the MIPS ADESPIKE routine.

A special effort was made to restore high-spatial-frequency information and correct for known light scattering within the camera system (Klaasen *et al.* 1997). As described in Helfenstein *et al.* (1996, Appendix I), this process requires that all images first be Fourier transformed. A restorative filter (MIPS WIENER program) is then used to deconvolve the wavelength-dependent modulation transfer functions and effects of random noise before the corrected images are inverted back to the spatial domain. Because the G7 images occupy less than a full 800 × 800 pixel frame and because the SSI scattered-light functions are significantly wider than the CCD chip dimensions (Klaasen *et al.* 1997), missing image data had to be filled-in and extended beyond the standard 800 × 800-pixel image frame boundaries prior to Fourier transforming. Otherwise, the scattering correction could introduce artifacts (darkening of the edges of the image) within a few pixels of the edge of Galileo coverage. Ideally, the missing image information should be filled-in by coverage that best matches the average brightness levels and albedo markings in the G7 scene.[9] No such Galileo coverage exists (the sole G1 picture of this region shows the features at very large incidence angles where albedo markings are strongly attenuated), however, Voyager images listed in Table I do show the G7 region at sufficiently small incidence angles and over a wide enough region (Fig. 3) to perform the correction. Standard methods were used to radiometrically calibrate the Voyager images. After determining the correct camera pointing geometry for each frame, the Voyager images were digitally remapped and photometrically renormalized to a 1600 × 1600-pixel frame size centered on and at the viewing perspective of the G7 images.

To photometrically normalize the Voyager images to the G7 lighting geometry, the average leading-side photometric model of Domingue *et al.* (1991) was adopted. If DN_{VGR} is the measured radiance factor at (x_{vgr}, y_{vgr}) in the Voyager data, then the model-predicted Galileo value is given by

$$DN_{pred} = DN_{VGR} \frac{r_m(i_{GLL}, e_{GLL}, \alpha_{GLL})}{r_m(i_{VGR}, e_{VGR}, \alpha_{VGR})},$$

where i_{VGR}, e_{VGR}, and α_{VGR} are, respectively, the incidence, emission, and phase angles for Voyager image pixel location (x_{VGR}, y_{VGR}), $r_m(i_{VGR}, e_{VGR}, \alpha_{VGR})$ is the radiance factor computed from the photometric model, and $r_m(i_{GLL}, e_{GLL}, \alpha_{GLL})$ is the model radiance factor computed for the photometric geometry corresponding to the same geographic location in a G7 Galileo image. This correction assumes that all terrains have the same photometric function and differ only in albedo.

Because of calibration differences between the Voyager and Galileo

[9] An alternative method is to fill in the missing data with model reflectance computed for average europan surface materials. This approach would be satisfactory for image boundaries bordering relatively bright terrains, but would contribute errors of a few percent in the reflectance of relatively dark materials that occur within a few pixels of the boundary of G7 coverage.

image systems, and more importantly because brightness contrasts among europan terrains vary significantly with wavelength- and terrain-specific photometric properties, an additional brightness and contrast adjustment is required. After applying the first-order correction, each Voyager image was remapped to the corresponding G7 image viewing perspective and linear regression analysis was performed on the brightness values in areas of mutual overlap of Voyager and Galileo coverage. The result was a simple linear brightness and contrast adjustment (with gain A and offset B)

$$DN_{norm} = A\ DN_{pred} + B$$

that was satisfactory for completing the photometric renormalization of Voyager images to Galileo lighting geometries. Each G7 image was embedded in its corresponding Voyager basemap image, the scattered-light correction was performed, and the corrected G7 portion was extracted for analysis.

ACKNOWLEDGMENTS

This study was supported by the Galileo Project and NASA Grant NSG 2084. The authors are especially grateful to Y. Shkuratov and R. M. Nelson for insightful reviews. We thank Brian Carcich for help with computing and Mary Roth for help with manuscript preparation.

REFERENCES

Akkermans, E., P. Wolf, R. Maynard, and G. Maret 1988. Theoretical study of the coherent backscattering of light by disordered media. *J. Phys.* **49,** 77–98.

Belton, M. J., J. W. Head III, A. P. Ingersoll, R. Greeley, A. S. McEwen, K. P. Klaasen, D. Senske, R. Pappalardo, G. Collins, A. R. Vasavada, R. Sullivan, D. Simonelli, P. Geissler, M. H. Carr, M. E. Davies, J. Veverka, P. J. Gierasch, D. Banfield, M. Bell, C. R. Chapman, C. Anger, R. Greenberg, G. Neukum, C. P. Pilcher, R. F. Beebe, J. A. Burns, F. Fanale, W. Ip, T. V. Johnson, D. Morrison, J. Moore, G. S. Orton, P. Thomas, and R. A. West. 1996. Galileo's first images of Jupiter and the Galilean satellites. *Science* **274,** 377–385.

Buratti, B. 1985. Application of a radiative transfer model to bright icy satellites. *Icarus* **61,** 208–217.

Buratti, B. J. 1991 Ganymede and Callisto: Surface textural dichotomies and photometric analysis. *Icarus* **92,** 312–323.

Buratti, B., and M. Golombek, 1988. Europa: Geologic implications of spectrophotometry. *Icarus* **75,** 437–449.

Buratti, B., J. Hillier, and M. Wang 1996. Lunar opposition surge: Observations by Clementine. *Icarus* **124,** 490–499.

Clark, B., P. Helfenstein, J. Veverka, M. Ockert-Bell, R. Sullivan, P. Geissler, C. Phillips, A. S. McEwen, R. Greeley, G. Neukum, T. Denk, K. Klaasen, and The Galileo SSI Team 1998. Multispectral terrain analysis of Europa from Galileo images. *Icarus* **135,** 95–106.

Davies, M. E., and F. Y. Katayama 1980. *Coordinates of Features on the Galilean Satellites.* Rand Corporation Publ. N-1617-JPL/NASA, Santa Monica, CA.

Davies, M. E., T. A. Hauge, F. Y. Katayama, and J. A. Roth 1979. *Control Networks for the Galilean Satellites: November 1979.* RAND Corporation Publ. R-2532-JPL/NASA, Santa Monica, CA.

Davies, M. E., T. R. Colvin, J. Oberst, W. Zeitler, P. Schuster, G. Neukum, A. S. McEwen, C. B. Phillips, P. C. Thomas, J. Veverka, M. J. S. Belton, and G. Schubert 1998. The control networks of the Galilean satellites and implications for global shape. *Icarus* **135,** 372–376.

Denk, T., G. Neukum, P. Helfenstein, M. J. S. Belton, K. C. Bender, P. Geissler, R. Greeley, J. W. Head, R. Jaumann, R. T. Pappalardo, and the Galileo SSI Team 1997. Disk-resolved spectral characteristics of Ganymede and Callisto. *Lunar Planet. Sci.* **28,** 899–900.

Domingue, D., B. Hapke, G. W. Lockwood, and D. T. Thompson 1991. Europa's phase curve: Implication for surface structure. *Icarus* **90,** 30–42.

Etemad, S., R. Thompson, M. Andrejco, S. John, and F. MacKintosh 1987. Weak localization of photons: Termination of coherent random walks by absorption and confined geometry. *Phys. Rev. Lett.* **59,** 1420–1423.

Fanale, F. P., J. C. Granahan, T. B. McCord, G. Hansen, C. A. Hibbitts, R. Carlson, D. Matson, A. Ocampo, L. Kamp, W. Smythe, F. Leader, R. Mehlman, R. Greeley, R. Sullivan, P. Geissler, C. Barth, A. Hendrix, B. Clark, P. Helfenstein, J. Veverka, M. J. S. Belton, K. Becker, and T. Becker 1998. Galileo's multi-instrument spectral view of Europa's surface composition. *Icarus*, submitted.

Finnerty, A., G. Ransford, D. Pieri, and K. Collerson 1981. Is Europa's surface cracking due to thermal evolution? *Nature* **289,** 24–27.

Geissler, P. E., R. Greenberg, G. Hoppa, A. McEwen, R. Tufts, C. Phillips, B. Clark, M. Ockert-Bell, P. Helfenstein, J. Burns, J. Veverka, R. Sullivan, R. Greeley, R. Pappalardo, J. W. Head III, M. J. S. Belton, and T. Denk 1998. Evolution of lineaments on Europa: Clues from Galileo multispectral imaging observations. *Icarus* **135,** 107–126.

Golombek, M., and E. Bruckenthal, 1983. Origin of triple bands on Europa. *Lunar Planet. Sci.* **XIV,** 251–252.

Greeley, R., R. Sullivan, J. Klemaszewski, K. Homan, J. Head III, R. Pappalardo, J. Veverka, B. E. Clark, T. Johnson, K. P. Klaasen, M. Belton, J. Moore, E. Asphaug, M. Carr, G. Neukum, T. Denk, C. R. Chapman, C. Pilcher, P. Geissler, R. Greenberg, and R. Tufts 1998. Europa: Initial Galileo geological observations. *Icarus* **135,** 4–24.

Greenberg, R., P. Geissler, G. Hoppa, B. R. Tufts, D. D. Durda, R. Pappalardo, J. W. Head, R. Greeley, R. Sullivan, and M. H. Carr 1998. Tectonic processes on Europa: Tidal stresses, mechanical response, and visible features. *Icarus* **135,** 64–78.

Hapke, B. 1986. Bidirectional reflectance spectroscopy IV: The extinction coefficient and the opposition effect. *Icarus* **67,** 264–280.

Hapke, B. 1990. Coherent backscatter and the radar characteristics of outer planet satellites. *Icarus* **88,** 407–417.

Hapke, B. 1993. *Theory of Reflectance and Emittance Spectroscopy*. Cambridge University Press, New York.

Hapke, B., R. Nelson, and W. Smythe 1993. The opposition effect of the Moon: The contribution of coherent backscatter. *Science* **260,** 509–511.

Hapke, B., R. Nelson, and W. Smythe 1998. The opposition effect of the Moon: Coherent backscatter and shadow-hiding. *Icarus* **133,** 89–97.

Helfenstein, P. 1986. Photometrically determined surface physical properties of terrains on Ganymede. *Lunar Planet. Sci.* **XVIII,** pp. 333–334. [Abstract]

Helfenstein, P., and J. Veverka 1987. Photometric properties of lunar terrains derived from Hapke's equation. *Icarus* **72,** 342–357.

Helfenstein, P., J. Veverka, P. C. Thomas, D. Simonelli, K. Klaasen, T. V. Johnson, F. Fanale, J. Granahan, and A. S. McEwen 1996. Galileo photometry of Asteroid 243 Ida. *Icarus* **120,** 48–65.

Helfenstein, P., J. Veverka, and J. Hillier 1997a. The lunar opposition effect: A test of alternative models. *Icarus* **128,** 2–14.

Helfenstein, P., J. Veverka, T. Denk, G. Neukum, J. W. Head, R. Pappalardo, and the Galileo Imaging Team 1997b. Dark-floor craters: Galileo constraints on a Ganymede regolith component. *Lunar Planet. Sci.* **XXVIII,** pp. 547–548.

Johnson, R. E, and T. I. Quickenden 1998. Photolysis and radiolysis of ice on outer Solar System bodies. *J. Geophys. Res.* **102,** 10,985–10,966.

Kadel, S. D., S. A. Fagents, J. E. Klemaszewski, R. Greeley, and the

Galileo Imaging Team 1997. Fissure eruptions on Europa—An alternative origin for trough-bounding ridge pairs. *EOS.*

Klaasen, K., M. Belton, H. Breneman, A. McEwen, M. Davies, R. Sullivan, C. Chapman, G. Neukum, C. Heffernan, A. Harch, J. Kaufman, W. Merline, L. Gaddis, W. Cunningham, P. Helfenstein, and T. Colvin 1997. Inflight performance characteristics, calibration, and utilization of the Galileo SSI Camera. *Opt. Eng.* **36,** 3001–3027.

Kravtsov Y., and A. I. Saichev 1982. Effect of double passage of waves in randomly inhomogeneous media. *Sov. Phys. Usp.* **25,** 494–508.

Luchitta, B. K., and L. A. Soderblom 1982. The geology of Europa. In *Satellites of Jupiter* (D. Morrison, Ed.), pp. 521–555. Univ. of Arizona Press, Tucson.

Luchitta, B. K., L. A. Soderblom, and H. M. Ferguson 1981. Structures on Europa. *Proc. Lunar Planet. Sci. Conf. 12th,* pp. 1555–1567.

Malin, M. 1980. Morphology of lineaments on Europa. IAU Coll. 57, *The Satellites of Jupiter*, No. 7-2. [Abstract]

McEwen, A. 1986. Exogenic and endogenic albedo and color patterns on Europa. *J. Geophys. Res.* **91,** 8077–8097.

Mishchenko, M. I. 1991. Polarization effects in weak localization of light: Calculation of the copolarized and depolarized backscattering enhancement. *Phys. Rev. B.* **44,** 12,597–12,600.

Mishchenko, M. I. 1992a. Enhanced backscattering of polarized light from discrete random media: Calculations in exactly the backscattering direction. *J. Opt. Soc. Am.* **9,** 978–982.

Mishchenko, M. I. 1992b. The angular width of the coherent backscatter opposition effect: An application to icy outer planet satellites. *Astrophys. Space Sci.* **194,** 327–333.

Mishchenko, M. I., and J. M. Dlugach 1992. The amplitude of the opposition effect due to weak localization of photons in discrete, disordered media. *Astrophys. Space Sci.* **188,** 151–154.

Mishchenko, M. I., and J. M. Dlugach 1993. Coherent backscatter and the opposition effect for E-type asteroids. *Planet. Space Sci.* **41,** 173–181.

Nelson, R. M., B. W. Hapke, W. D. Smythe, and L. J. Spilker 1997. Experimental tests of models of the coherent backscattering opposition effect. *Lunar Planet. Sci.* **XXIX.**

Nozette, S., L. P. Pleanance, D. M. Horan, P. Regeon, E. M. Shoemaker, P. D. Spudis, C. H. Acton, D. N. Baker, J. E. Blamont, B. J. Buratti, M. P. Corson, M. E. Davies, T. C. Duxbury, E. M. Eliason, B. M. Jokosky, J. F. Kordas, I. T. Lewis, C. L. Lichtenberg, P. G. Lucey, E. Malaret, M. A. Massie, J. H. Resnick, C. J. Rollins, H. S. Park, A. S. McEwen, R. E. Priest, C. M. Pieters, R. A. Reisse, M. S. Robinson, R. A. Simpson, C. E. Smith, T. C. Sorenson, R. W. Vorder Breugge, and M. T. Zuber 1994. The Clementine mission to the Moon: Science Overview. *Science* **266,** 1835–1839.

Oetking, P. 1966. Photometric studies of diffusely reflecting surfaces with applications to the brightness of the Moon. *J. Geophys. Res.* **71,** 2505–2513.

Pappalardo, R. T., and R. J. Sullivan 1996. Evidence for separation across a gray band on Europa, *Icarus* **123,** 557–567.

Pappalardo, R. T., J. W. Head, G. Collins, R. Greeley, C. Pilcher, G. Schubert, W. B. Moore, M. Carr, J. M. Moore, M. J. S. Belton, and D. Goldsby 1998. Geological evidence for solid state convection in Europa's ice shell. *Nature* **391,** 365–368.

Pohn, H. A., H. W. Radin, and R. L. Wildey 1969. The Moon's photometric function l, near zero phase angle from Apollo 8 photography. *Astrophys. J* **157,** L193–L195.

Shkuratov, Y. G. 1985. On the origin of the opposition effect and negative polarization for cosmic bodies with solid surfaces. *Astron. Circ.* 1400, 3–6.

Shkuratov, Y. G. 1988. A diffraction mechanism of the opposition effect of a surface with complicated structure. *Kinemat. Fiz. Nebesn. Tel.* **4**(4), 33–39.

Shkuratov, Y. G. 1991. Estimating the effect of angular light source dimensions on the opposition brightness effect of atmosphereless bodies. *Solar System Res.* **25**(1), 54–57.

Shkuratov, Y. G. 1995. Can the lunar opposition spike measured by Clementine exist? *Lunar Planet. Sci.* **XXIV,** 1295–1296.

Shkuratov, Y. G., M. A. Kreslavsky, and D. G. Stankevich 1997. On the lunar opposition spike observed by Clementine. *Lunar Planet. Sci.* **XXVI,** 1307–1308.

Shkuratov, Y. G., L. Y. Melkumova, N. V. Opansenko, and D. G. Stankevich 1996. Phase dependence of the color indices of solid surfaces of celestial bodies. *Solar System Res.* **30,** 71–79.

Shkuratov, Y. G., N. V. Opanasenko, A. T. Basilevsky, B. S. Zhukov, M. A. Kreslavsky, and S. Murchie 1991. A possible interpretation of bright features on the surface of Phobos. *Planet. Space Sci.* **39,** 341–347.

Shkuratov, Y. G., A. A. Ovcharenko, D. G. Stankevich, and V. V. Korokhin 1997. A study of light backscattering from planetary-regolith-type surfaces at phase angles 0.2–3.5 degrees. *Solar System Res.* **31,** 56–63.

Smith, B. A., L. A. Soderblom, R. Bebee, J. Boyce, G. Briggs, M. Carr, S. A. Collins,. A. F. Cook, G. E. Danielson, M. E. Davies, G. E. Hunt, A. Ingersoll, T. V. Johnson, H. Masursky, J. McCauley, D. Morrison, T. Owen, C. Sagan, E. M. Shoemaker, R. Strom, V. E. Soumi, and J. Veverka 1979. The Galilean satellites and Jupiter: Voyager 2 imaging results. *Science* **206,** 927–950.

Spencer J. R., L. Prockter, R. Pappalardo, J. W. Head III, and J. Moore 1998. Local volatile migration on Ganymede: Galileo SSI images, PPR radiometry, and theoretical considerations. *Lunar Planet. Sci.* **XXIX,** abstract no. 1149, Lunar and Planetary Institute, Houston. [CD-ROM]

Sullivan, R., M. Belton, M. Carr, C. Chapman, B. Clark, P. Geissler, R. Greeley, R. Greenberg, J. Head, J. Klemaszewski, M. Kraft, J. Moore, J. Moreau, R. Pappalardo, C. Pilcher, B. R. Tufts, K. Williams, and the Galileo SSI Team 1997. Ridge formation on Europa: Examples from Galileo high resolution images. *Geol. Soc. Am. Abstracts Programs.* **29**(6), A-312.

Thompson, D. T., and G. W. Lockwood 1992. Photoelectric photometry of Europa and Callisto. *J. Geophys. Res.* **97,** 14,761–14,772.

Van Albada, M., M. Van der Mark, and A. Lagendijk 1990. Experiments on weak localization of light and their interpretation. In *Scattering and Localization of Classical Waves in Random Media* (P. Sheng, Ed.), pp. 97–136. World Scientific, Teaneck, NJ.

Verbiscer, A., and P. Helfenstein 1998. Reflectance spectroscopy of icy surfaces. In *Solar System Ices* (B. Schmitt, C. de Bergh, and M. Festou, Eds.), Astrophys. Space Sci. Library, Vol. 227. Kluwer Academic, Dordrect.

Veverka, J., P. Thomas, T. V. Johnson, D. Matson, and K. Housen 1986. The physical characteristics of satellite surfaces. In *Satellites* (J. A. Burns and M. S. Matthews, Eds.), pp. 372–402. Univ. of Arizona Press, Tucson.

Whitaker, E. 1969. An investigation of the lunar heiligenschein. In *Analysis of Apollo 8 Photography and Visual Observations*, pp. 38–39. NASA SP-201.